Deciphering the Morphology of Transition Metal Carbonate Cathode Precursors

Pallab Barai[1], Xiaoping Wang[2], Mark Wolfman[3], Jiajun Chen[2], Arturo Gutierrez[2], Juan C. Garcia[2], Jianguo Wen[4], Tiffany Kinnibrugh[2], Timothy T. Fister[2], Hakim H. Iddir[2], and Venkat Srinivasan[5*]

[1]Applied Materials Division, Argonne National Laboratory, Lemont, IL 60439 USA

[2]Chemical Sciences and Engineering Division, Argonne National Laboratory, Lemont, IL 60439 USA

[3]Advanced Photon Source, Argonne National Laboratory, Lemont, IL 60439 USA

[4]Center for Nanoscale Materials, Argonne National Laboratory, Lemont, IL 60439 USA

[5]ACCESS, Argonne National Laboratory, Lemont, IL 60439 USA

Revised version for submission in

Journal of Materials Chemistry A

March 2024

*Corresponding author: Venkat Srinivasan (vsrinivasan@anl.gov)

Abstract

The performance and life of Li-ion battery cathode materials is determined by both the composition (crystal structure and transition metal ratio) and the morphology (particle size, size distribution, and surface area). Careful control of these two aspects is the key to long lasting, high-energy batteries that can undergo fast charge. Developing such cathodes requires manipulation of the synthesis conditions, namely the coprecipitation process to develop precursor and calcination step to lithiate and convert it to the transition metal oxide. In this paper, we utilize a combination of controlled synthesis, microscopic and spectroscopic characterization, and multi-scale mathematical modeling to shed light into the synthesis of cathode precursors. The complex interplay between the various chemical reactions in the co-precipitation process is studied to provide experimentalist with guidance on achieving composition control during synthesis. Further, the formation of a variety of morphologies of the primary particles and the driving force for agglomeration is mathematically described, for the first time, based on an energy minimization approach. Results suggest that presence of Ni and/or Co significantly lowers the reaction rate constant compared to Mn, resulting in agglomerated growth in the former and single crystal growth in the latter. The modeling studies are used to provide a phase map describing the synthesis conditions needed to control the secondary particle size and corresponding size distribution. This paper represents an important step in developing a computationally guided approach to synthesis of battery cathode materials.

Introduction

With the need to continuously improve the energy density of current lithium-ion batteries (LIB), there is a growing trend towards developing new high-capacity cathode and anode materials.[1-3] This trend has been augmented by the growing supply chain challenges for critical battery materials, specifically cobalt (Co) due to its high cost.[4] The community has rapidly moved towards increasing the nickel (Ni) in the $LiNi_xMn_yCo_zO_2$ (x+y+z=1) cathodes (also known as NMC cathodes) to minimize the amount of cobalt, with NMC-811 an increasing popular choice.[5-7] However, in the past year, there has been growing concern around the use of nickel.[8-11] This in turn has spurred interest in manganese-rich cathodes, with growing interest in the $xLi_2MnO_3 \cdot (1-x)LiMO_2$ (or LMR-NMC), etc.[12-15] composition, with material-level specific energy around 900 Wh/kg, while charged to a 4.7 V.[16, 17]

While promising, both NMC-811 and LMR-NMC, suffer from multiple challenges.[18-23] NMC-811 is known to have high reactivity due to the high Ni content, along with a significant molar volume change at high state of charge (SOC), which in turn leads to particle cracking.[22, 24] Alleviating these issues requires minimizing the surface area of the cathode, and minimizing the grain boundaries, which serve as the nucleation point for cracks.[25] On the other hand, LMR-NMC is known to have a poor diffusion for Li ions in the lattice (10^{-11} – 10^{-17} cm^2/s vs 10^{-10} cm^2/s in NMC).[20] This necessitates the use of small primary particles to minimize diffusion lengths, while not compromising on the tap density or the reactivity of the cathode.[20] To address these challenges, the research community is focused on synthesis approaches that can lead to the precise composition and morphology of the material in order to maximize the energy density while minimizing side reactions.[26] Note that various coating strategies have also been investigated in the literature to minimize surface reactivity, which is not addressed in the present study.[7, 27]

Typical synthesis of TM cathodes, such as LMR-NMC, involves two steps. In the first step Mn-rich carbonate precursors are precipitated using the coprecipitation techniques.[16, 28, 29] In the second step these Mn-rich carbonate precursors are calcined at elevated temperatures with excess lithium salt that oxidizes and lithiates the precursor materials and leads to the formation of LMR-NMC cathode particles.[30] Final performance of a battery cathode material depends on two aspects:[31-33]

a) The atomic crystal structure that determines the maximum cell voltage and lithium capacity under thermodynamic equilibrium configuration.[33]
b) Morphology of the cathode particles, such as, size of the primary and secondary particles, size distribution, internal porosity, etc., which determines the kinetic and transport limitations that prevent the cell from achieving its maximum thermodynamically feasible performance.[20]

The coprecipitation process has the advantage that it holds the possibility of attaining atomic level mixing of the transition metals.[34, 35] Coprecipitation of cathode precursors produce secondary particles that consists of smaller primary particles.[34, 36] During the high temperature calcination process, even though the primary particle morphology of the cathodes undergoes substantial changes, the size and size distribution of the secondary particles remain close to those obtained from the coprecipitation process.[37, 38] In addition, the morphology of the primary particles in the cathode precursors impacts the rate of oxidation and lithiation reactions that occur during the high temperature calcination.[39] Therefore, understanding and controlling the co-precipitation step remains an important aspect for control of the material.

While similar considerations are important when synthesizing nickel rich NMCs, the specific conditions and approaches change substantially. For example, the synthesis of Ni-rich cathodes utilizes hydroxide based precursors[40], in contrast to Mn rich cathodes which utilize

carbonate based precursors. In Mn rich cathodes, hydroxide based precursors tend to oxidize to oxyhydroxides, which can act as an impurity.[34] After coprecipitation, to maintain Mn in a +2 oxidation state, Mn-rich cathodes are synthesized through the precipitation of carbonate based precursors.[34]

The intimate link between the synthesis method and the final composition and the morphology of the cathode precursors is generally conducted in a trial-and-error approach. In this paper, we take a systematic approach to understand the underlying physics that governs the synthesis and develop a mathematical framework, aided by experimental data, to bring new perspectives to the problem. This paper builds on an earlier work by the authors that focused solely on $MnCO_3$ precursors, and the corresponding evolution of the primary and secondary particles.[41] In the present study, precipitation of Ni, Co, and NMC (with equal amount of Ni, Co and Mn) carbonate precursors is investigated to complete the picture on the dynamics during co-precipitation. Experimental data shows that the choice of the TM significantly impacts the particle morphology and composition.

Understanding these dynamics is aided by the development of a multiscale model. The fundamental principle that governs the coprecipitation of cathode precursors is minimization of energy.[42] After mixing all the reactants in the solution, the supersaturation ratio of the desired precipitate (i.e., transition metal carbonate or $TMCO_3$), increases substantially leading to a rapid increase in the free energy of the system.[43] Both the nucleation and the growth of these precursor particles occur to minimize the supersaturation ratio and effective free energy of the reacting solution.[44] Due to the variation in precipitation conditions and the presence of alternate anions (for example, OH^- while precipitating $TMCO_3$), it is possible to form various transition metal impurities (such as, transition metal hydroxides or $TM(OH)_2$) that can substantially influence the

precipitation of the desired $TMCO_3$ precursors.[43, 45] As depicted in Figure 1, after the initial nucleation, growth of the particles during the precipitation process can occur through three different routes:[41, 46]

a) Direct precipitation on top of a pre-existing single crystalline particle results in its further growth, which is usually observed in precipitates with larger reaction rate constant.
b) On the other hand, precipitates with smaller reaction rate, cannot lead to the formation of large sized single crystalline particles. Rather, heterogeneous nucleation on top of the surface of a pre-existing particle is a preferred mode of growth for these precipitates, which results in formation of surface particles. This effective growth mechanism is associated with the surface nucleation process, and hence characterized as the surface growth phenomena.
c) Agglomeration of multiple primary particles, or primary aggregates, can lead to minimization of the surface energy, and the total free energy of the system would decrease.

Accordingly, the precipitation mechanism of cathode precursors involves multiple phenomena, such as, nucleation, direct growth, surface growth through heterogeneous nucleation on surface, and possibly agglomeration of multiple precipitates.[47] The reaction rate constant associated with the precipitation of the $TMCO_3$ can depend on the water exchange rate constants, which differs substantially for Ni^{2+}, Mn^{2+}, and Co^{2+} in aqueous solution.[48] The final particle morphology (such as, particle size, size distribution, internal porosity, BET surface area, etc.) depends substantially on either the dominant or the limiting mechanism of growth. Whether a precipitate will take its thermodynamically equilibrium Wulff configuration is dictated by the rate associated with the re-orientation of molecules, which is known as the "orientation velocity" or the "surface diffusivity".[41, 44] Presence of impurity phases during the precipitation of $TMCO_3$ can alter their

rates of precipitation, or the magnitudes of "surface diffusivity" influencing its ability to achieve the Wulff shape. Propensity of formation of the Wulff shape during the coprecipitation of $MnCO_3$ was investigated earlier,[41] which is not being pursued in the present study for other transition metal carbonates. Morphology of the primary and secondary particles, and their corresponding growth mechanisms, for the individual Ni and Co based transition metal carbonate precursors, and the same for NMC111 carbonates, will be investigated as part of the present study.

Note that all the precipitation experiments, and corresponding computational analysis, will be conducted in a batch reactor, typically used in most academic settings.[41, 49] Industrial reactors differ from research reactors, where the former is driven by the need for larger product volumes. The fundamental understanding of the coprecipitation mechanisms obtained from this study can be transferred to the coprecipitation in industrially relevant reactors such as continuous stirred tank (CSTR) and Taylor vortex (TVR) reactors.[16, 40, 50]

Methodology

Experimental precipitation and detailed imaging of the transition metal carbonate precursors were conducted as part of this study. Two sets of computational models were developed, where the first one is used to predict the composition of the precipitates, and the second model helps to capture the morphology of the precipitated particles.

Experimental precipitation of the transition metal carbonates: Precipitation of $NiCO_3$, $CoCO_3$ and $NMC111CO_3$ were conducted in a batch reactor by following the procedure reported in an earlier paper published by the authors to precipitate $MnCO_3$ cathode precursors.[41, 49] Two different solutions were prepared in DI water, the first one being 1.2 L of the desired transition metal sulfate in 4.5 mM concentration ($NiSO_4$ for precipitating $NiCO_3$, $CoSO_4$ for precipitating

$CoCO_3$, or a mixture of $NiSO_4$, $CoSO_4$ and $MnSO_4$ in equal amount for precipitating $NMC111CO_3$), and the second one being 1.2 L of NH_4HCO_3 solution with desired concentration. $CoCO_3$ and $NMC111CO_3$ were precipitated with ammonia over transition metal ratio of 40 ($[NH_4^+]/[TM^{2+}] \sim 40$), whereas $NiCO_3$ was precipitated with $[NH_4^+]/[TM^{2+}]$ ratio of 15. Both the solutions were preheated to 50^0C before mixing in a 4 L reactor, where the precipitation was allowed to continue in a batch mode for 1 hour at 50^0C under a stirring speed of approximately 500 rpm to obtain good mixing of the reactants.[49] Due to the buffering mechanism of ammonia, the solution pH was maintained around 7.5 (no pH controller was installed during the precipitation process).[41, 49] All the samples were collected at the end of the 1 hour long precipitation process, which were then washed and dried in an oven overnight at 110^0C under flowing nitrogen to prevent any unwanted oxidation of the carbonate precursors.

SEM and TEM imaging techniques: Both low and high resolution imaging of the precipitated transition metal carbonate precursors were conducted to elucidate the morphology of the secondary and primary particles. Morphology of the precipitated secondary particles was examined using a JEOL NeoScope JCM-6000Plus Scanning Electron Microscope (SEM) at a relatively lower resolution (scale bar around 2 μm – 50 μm).[51] The same instrument was also used to determine the distribution of transition metals near the surface of the precursor particles through the Energy Dispersive X-ray (EDX) mapping technique. To understand its primary particle morphology, high resolution scanning transmission electron microscopy (STEM) images of the transition metal carbonate particles were taken using the Talos F200X TEM and Argonne Chromatic Aberration-corrected TEM (ACAT) instruments (scale bar around 2 nm – 50 nm).[52]

Powder X-ray Diffraction: Powder samples were loaded as-is into Kapton capillaries and measured at beamline 17-BM of the Advanced Photon Source (APS in Argonne National Lab).

Patterns were measured with the beamline's Varex 4343CT area detector. Calibration was performed against a LaB_6 reference sample using Dioptas software.[53] The beamline wavelength was determined to be 0.45175Å and the detector distance was 534 mm from the sample. Reduction of area detector patterns to one-dimensional patterns was performed using Dioptas.

Atomistic simulations: All atomistic calculations were performed using spin-polarized Density Functional Theory (DFT) via the Vienna Ab Initio Simulation Package (VASP).[54, 55] For exchange-correlation potentials, the Generalized Gradient Approximation (GGA) as formulated by Perdew, Burke, and Ernzerhof (PBE) were applied.[56] To model the interaction between the valence electrons and the atomic cores, the Projected Augmented Wave (PAW) method were utilized.[57] Additionally, the GGA+U approach were incorporated to account for the on-site electron correlation in the 3d orbitals of the transition metals (TM), setting the (U−J) parameter to 5.96 eV for Nickel (Ni), 5.00 eV for Cobalt (Co), and 4.84 eV for Manganese (Mn).[58] The wave functions were expanded using a plane wave basis with a kinetic energy cut-off of 500 eV. A repeating slab model was introduced with vacuum separation to prevent inter-slab interactions, choosing a vacuum gap of 12 Å. The supercell lattice parameters were maintained at the bulk value throughout the simulations. The ions within the supercell were allowed to relax until the total energy variance between steps was less than 0.003 eV.

Equilibrium analysis to understand the composition of transition metals within the precipitate: Different transition metal sulfates ($NiSO_4$, $MnSO_4$ and $CoSO_4$) were mixed in desired amount with NH_4HCO_3 to precipitate the desired transition metal carbonates.[41, 49] In order to elucidate the transition metal composition within the precipitates, it is necessary to understand the thermodynamics governing the entire precipitation process.[59] Due to their very high solubility in water, all the transition metal sulfates ($TMSO_4$) and the NH_4HCO_3 do completely dissolve in

water and dissociate into their respective cations and anions. The total concentration of Ni^{2+}, Mn^{2+}, and Co^{2+} in the reactor is denoted by $\bar{c}_{Ni^{2+}}$, $\bar{c}_{Mn^{2+}}$, and $\bar{c}_{Co^{2+}}$, respectively, the total concentration of bicarbonate anions is given by $\bar{c}_{HCO_3^-}$, and the total concentration of ammonia is denoted as $\bar{c}_{NH_3}$. Mass balance for each of the individual species is satisfied (as provided below), to determine the final concentration of the precipitated transition metal carbonates ($NiCO_3$, $MnCO_3$ and $CoCO_3$) and transition metal hydroxides ($Ni(OH)_2$, $Mn(OH)_2$ and $Co(OH)_2$).[28, 59-61]

$$\bar{c}_{Ni^{2+}} = [Ni^{2+}] + [NiCO_3] + [Ni(OH)_2] + [Ni(NH_3)]^{2+} + [Ni(NH_3)_2]^{2+} + [Ni(NH_3)_3]^{2+} + [Ni(NH_3)_4]^{2+} + [Ni(NH_3)_5]^{2+} + [Ni(NH_3)_6]^{2+} \quad (1)$$

$$\bar{c}_{Mn^{2+}} = [Mn^{2+}] + [MnCO_3] + [Mn(OH)_2] + [Mn(NH_3)]^{2+} + [Mn(NH_3)_2]^{2+} + [Mn(NH_3)_3]^{2+} + [Mn(NH_3)_4]^{2+} \quad (2)$$

$$\bar{c}_{Co^{2+}} = [Co^{2+}] + [CoCO_3] + [Co(OH)_2] + [Co(NH_3)]^{2+} + [Co(NH_3)_2]^{2+} + [Co(NH_3)_3]^{2+} + [Co(NH_3)_4]^{2+} + [Co(NH_3)_5]^{2+} + [Co(NH_3)_6]^{2+} \quad (3)$$

$$\bar{c}_{HCO_3^-} = [HCO_3^-] + [H_2CO_3] + [CO_3^{2-}] + [NiCO_3] + [MnCO_3] + [CoCO_3] \quad (4)$$

$$\bar{c}_{NH_3} = [NH_3] + [NH_4^+] + [Ni(NH_3)]^{2+} + 2[Ni(NH_3)_2]^{2+} + 3[Ni(NH_3)_3]^{2+} + 4[Ni(NH_3)_4]^{2+} + 5[Ni(NH_3)_5]^{2+} + 6[Ni(NH_3)_6]^{2+} + [Mn(NH_3)]^{2+} + 2[Mn(NH_3)_2]^{2+} + 3[Mn(NH_3)_3]^{2+} + 4[Mn(NH_3)_4]^{2+} + [Co(NH_3)]^{2+} + 2[Co(NH_3)_2]^{2+} + 3[Co(NH_3)_3]^{2+} + 4[Co(NH_3)_4]^{2+} + 5[Co(NH_3)_5]^{2+} + 6[Co(NH_3)_6]^{2+} \quad (5)$$

All the above-mentioned equations are solved simultaneously using the Newton-Raphson method. Concentrations of protons (H^+) and hydroxyl anions (OH^-) are determined from the pH of the reactor, which is considered as an input to the computational model. The chemical reactions and corresponding equilibrium constants are provided in Table S1 within the Supplementary Information section.

According to the existing literature, precipitation of transition metal carbonates ($TMCO_3$), which can be either $NiCO_3$, $MnCO_3$, or $CoCO_3$, or a mixture of the three ($NMC111CO_3$), can occur through two different possible chemical reaction pathways:[59, 60, 62-64]

i) Reaction I: The first scenario is the reaction between transition metal ammonia complex and carbonate anions:

$$[TM(NH_3)_n]^{2+} + CO_3^{2-} \rightleftharpoons TMCO_3 + nNH_3 \quad (8)$$

ii) Reaction II: The second possibility is direct reaction between the transition metal cations and carbonate anions:

$$TM^{2+} + CO_3^{2-} \rightleftharpoons TMCO_3 \quad (9)$$

In the present research, the dominant mechanism will be determined through appropriate comparison with experimentally observed distribution of Ni, Mn, and Co in the precipitated transition metal carbonates ($TMCO_3$).

Computational framework to simulate the growth of transition metal carbonate ($TMCO_3$) *primary particles and primary aggregates:* The primary particle morphology of the transition metal carbonates is extracted from the high resolution SEM and TEM images. To elucidate their formation mechanism, a lattice based computational framework, inspired by the Monte Carlo techniques, is developed that can successfully capture the evolution of primary particles and their aggregates.[65, 66] Formation of the primary particle aggregates is assumed to occur through the surface nucleation mechanism. Different rate constants are defined for capturing the growth of the primary particles (k_{pp}), primary particle aggregates (k_{ppa}), and rate of surface nucleation (k_{sn}). All these physical processes of surface nucleation and growth are proportional to the supersaturation ratio (SSR) of the $TMCO_3$ within the reactor. Supersaturation ratio is defined as the ratio between the product of the reactants over the solubility product,[47, 67]

$$SSR = [\mathrm{TM}^{2+}] \cdot [\mathrm{CO}_3^{2-}] / K_{\mathrm{SP,TMCO_3}} \quad (10)$$

where $[\mathrm{TM}^{2+}]$ indicates the concentration of free transition metal cations floating within the solution, $[\mathrm{CO}_3^{2-}]$ denotes the concentration of carbonate anions, both in $\mathrm{mol/L}$ units, and $K_{\mathrm{SP,TMCO_3}}$ indicates the solubility product of the corresponding transition metal carbonate. Please check the Supplementary Information section for the detailed equations that govern the growth of the primary particles and primary aggregates.

Nucleation of surface particles is a very important phenomena that controls the morphology or roughness of the surface of the primary particle aggregates. Evolution of a new nuclei is expected to occur in such a way that the increase in surface energy is minimum, which can also be written as:[42]

$$\min\left(E_{\mathrm{surf,tot}}\right) = \min\left((a_{\mathrm{ss}} \cdot \gamma_{\mathrm{ss}}) + (a_{\mathrm{sl}} \cdot \gamma_{\mathrm{sl}})\right) = \max(a_{\mathrm{ss}}) \cdot \gamma_{\mathrm{ss}} + \min(a_{\mathrm{sl}}) \cdot \gamma_{\mathrm{sl}} \quad (11)$$

Here a_{ss} and a_{sl} indicate the surface area between the solid-solid and solid-liquid interfaces, respectively, and γ_{ss} and γ_{sl} denote the surface energy density at the solid-solid and solid-liquid interface, respectively. The second equality in Eq. (11) holds because the surface energy between two solids is always assumed to be smaller than the surface energy between solids and liquids $(\gamma_{\mathrm{ss}} < \gamma_{\mathrm{sl}})$.

Note that finding the exact location that minimizes the solid-liquid contact area $(\min(a_{\mathrm{sl}}))$ is not trivial and requires physical time. In the present computational framework, it is assumed that the diffusion of transition metal within the reacting solution (governed by the diffusion coefficient D_{TM}) helps to find the location which minimizes a_{sl}. Amount of time available (Δt) before the formation of a surface nucleus is assumed to be inversely proportional to the rate coefficient of surface nucleation (k_{sn}) and supersaturation ratio (SSR).[68]

$$\Delta t = 1/(k_{\mathrm{sn}} \cdot SSR) \quad (12)$$

As already mentioned earlier, the implemented computational methodology assumes that the exact location that minimizes the surface energy is determined through the diffusion of transition metal within the reacting solution. Hence, the distance (Δx) over which the searching for the minimum energy location is conducted is given by:

$$\Delta x = \sqrt{D_{\mathrm{TM}} \cdot \Delta t} \tag{13}$$

Precipitation of transition metal carbonates with extremely high supersaturation ratio should get less time to search for the minimum energy location, whereas transition metal carbonates with smaller supersaturation should have more time to look for the minimum energy configuration. Accordingly, precipitates formed under higher magnitudes of SSR should demonstrate larger number of high energy solid-liquid interface, whereas precipitation under lower SSR should form less amount of the high energy solid-liquid interface. More details of the computational methodology adopted to capture the evolution of the primary particles and primary aggregates can be found in the Supplementary Information section.

Computational framework to capture the evolution of transition metal carbonate ($TMCO_3$) *secondary particles:* Particle size and size distribution are the two major morphological features of the transition metal carbonate ($\mathrm{TMCO_3}$) secondary particles that are widely investigated, which are also easy to estimate using low resolution benchtop SEMs and/or particle size analyzers (PSA).[50, 69] In the present study, evolution of the transition metal carbonate secondary particles is predicted using a Kinetic Monte Carlo (KMC) based technique, where agglomeration of the primary particle aggerates (ppa) is assumed to give rise to the spherical secondary particles.[46] Note that from an experimental standpoint, it is very difficult to differentiate between the primary aggregates and secondary particles, as both of them would appear very similar, which looks like aggregates of very small nanometer sized primary particles. Based on the reaction rate constants

for primary particles (k_{pp}) and primary particle aggregates (k_{ppa}), the maximum possible size of primary particle aggregates is around 1 μm – 2 μm after conducting coprecipitation for 1 hour (parameters provided in Table S2 in the Supplementary Information section). However, the size of the secondary particles, obtained after the completion of the coprecipitation in the batch reactor, is around 5 μm – 6 μm, which clearly indicates that further agglomeration of the primary aggregates must be taken into consideration for successfully predicting the appropriate size of the secondary particles.

Growth of the primary particle aggregates is assumed to occur according to Eqs (S3) to (S6) and Table S2 provided in the Supplementary Information section. Within the batch reactor, these primary particle aggregates float around due to the stirring induced convective motion, as well as the Stokes-Einstein diffusion process, whichever provides faster movement of the primary particle aggregates.[70-72] The Stokes-Einstein diffusivity depends inversely on the particle size, which is discussed in detail in the Supplementary Information section.

During their random movement, if one of the primary particle aggregate encounters another primary particle aggregate, or a secondary particle, it is assumed that they collide and merge with each other with a certain probability.[73, 74] Magnitude of this probability for agglomeration is a function of the surface energy between solid and liquid (γ_{sl}) and the size of the smaller particle.[46] Similar merging of two secondary particles is also possible if their size is small enough that allows for the agglomeration process. Overall, random movement of the primary particle aggregates and secondary particles, and their agglomeration under favorable condition, results in the evolution of the $\mathrm{TMCO_3}$ secondary particles.[75] More details about the agglomeration mechanism are provided within the Supplementary Information section. Size and

size distribution of these computationally predicted secondary particles are estimated and compared with the experimental observations.

Results and Discussion

In this work, coprecipitation of $MnCO_3$, $CoCO_3$, $NiCO_3$, and $NMC111CO_3$ was conducted using a batch reactor; the chemical composition and the morphology of the precipitated particles were investigated using experimental characterization techniques and explained using computational means. The following aspects will be discussed in the subsequent manuscript:

a) Precipitation of $TMCO_3$ cathode precursors and their secondary particle morphology
b) Driving force for precipitation experienced by different transition metal carbonates
c) Chemical composition of precipitates and corresponding reaction mechanism
d) Morphology of the precipitated primary particles and the primary particle aggregates
e) Computational simulation of time evolution of the secondary particle morphology

All the experimental precipitation and characterization was conducted using the techniques mentioned in the Methodology section. The corresponding computational analyses, to decipher the precipitation process, were conducted using the computational methodology provided in the Methodology and Supporting Information (SI) section, while using the parameters given in Tables S1 – S3.

Precipitation of $TMCO_3$ cathode precursors and their secondary particle morphology: As described in the Methodology section, the $TMCO_3$ cathode precursors are precipitated in a batch reactor by mixing $TMSO_4$ with NH_4HCO_3 over a time interval of 1 hour where the solution in the reactor was continuously stirred at 500 rpm.[49] NH_4^+ over TM^{2+} ratio was maintained at 40 $\left(([NH_4^+]/[TM^{2+}])\sim 40\right)$ except for the case of $NiCO_3$, where ammonia over nickel ratio was

maintained at 15 ($([NH_4^+] / [Ni^{2+}]) \sim 15$). Smaller concentration of ammonium bicarbonate was adopted while precipitating $NiCO_3$ because of the higher tendency to form the nickel-ammonia complex ($[Ni(NH_3)_n]^{2+}$) at high concentration of ammonium ion.[59] Consumption of large amount of ammonia in the form of nickel-ammonia complex can substantially decrease the concentration of free nickel ions ($[Ni^{2+}]$) within the solution, which is needed for reacting with the carbonate anions to form the $NiCO_3$ precipitate (see the reaction shown in Eq. (8) in the Methodology section). The other transition metals (Mn^{2+}, Co^{2+} and $[NMC111]^{2+}$) demonstrate lower propensity to form the $[TM(NH_3)_n]^{2+}$ complex, which results in precipitation of substantial amount of the $TMCO_3$ even with larger amount of ammonia $\left(([NH_4^+]/[TM^{2+}]) \sim 40\right)$.[64] Note that the concentration of $TMSO_4$ was maintained at 4.5 mM for all the precipitates.

Morphology of the various transition metal carbonate precipitates, as characterized by standard benchtop scanning electron microscopy (SEM), is provided in Figure 2. The scale bar for all the images is around 10 μm, which indicates that the morphology of the particles being characterized reveals secondary particles of the corresponding $TMCO_3$. It is evident from Figure 2(a) that the $MnCO_3$ secondary particles look like single crystals, or pseudo single crystals.[41, 49] Majority of these $MnCO_3$ appear to be cubic in shape, but some of them look spherical, and some others show rhombohedral shapes. Size of these $MnCO_3$ secondary particle range between 4 – 8 μm (for more information about the precipitation of $MnCO_3$ in a batch reactor, the readers are requested to refer to Garcia et al. Chem. Mater. (2020)).[41] It was argued by the authors that with increasing concentration of the Mn^{2+} cations, a competition between the thermodynamics and kinetics of precipitation leads to the formation of the rhombohedral, cubic, and spherical shaped $MnCO_3$ secondary particles .[41]

Morphology of the secondary particles as characterized through benchtop SEM, for $CoCO_3$, $NiCO_3$, and $NMC111CO_3$, is demonstrated in Figures 2(b), 2(c), and 2(d), respectively. It is evident from Figure 2(b) that $CoCO_3$ forms rough and random shaped secondary particles, with size in the range of 1 – 3 μm.[76] The rough surface of these $CoCO_3$ secondary particles indicate some form of agglomeration or surface growth mechanism. It is evident from Figure 2(c) that the secondary particle surface of $NiCO_3$ also appears to be rough, which is very similar to that observed for $CoCO_3$, and indicates growth through surface nucleation and/or aggregation process. The size of the $NiCO_3$ secondary particles appear to be around 0.5 – 3 μm, which is approximately similar to that observed for $CoCO_3$. Interestingly, Figure 2(d) shows that the $NMC111CO_3$ particles are smoother and more spherical in shape, with size in the range of 5 – 6 μm.[64] The spherical appearance indicates that these $NMC111CO_3$ secondary particles must be agglomeration of very small sized primary particles, which effectively end up forming a smooth surface. Note that all the surface roughness being alluded to in the present context is observed from SEM images with a scale bar of 10 μm. Higher resolution images can possibly reveal different morphological features, which is not evident at such large length scales. High resolution imaging of the primary particles and primary aggregates will be addressed later in this article.

Driving force for precipitation experienced by different transition metal carbonates: The morphology of $TMCO_3$ particles demonstrated in Figure 2 is dictated by the mechanism behind the precipitation process. A major driving force that substantially impacts the rate of precipitation is the supersaturation ratio (SSR).[41, 46] For the precipitation of transition metal carbonates, the supersaturation ratio (SSR) is defined as the ratio between the concentration of reactants $([TM^{2+}], [CO_3^{2-}])$ over the solubility product $\left(K_{SP,TMCO_3}\right)$ of that compound in the solvent where the precipitation is occurring (see Eq. (10) in the Methodology section for a detailed definition).

For all the four types of transition metals ($Mn^{2+}, Ni^{2+}, Co^{2+}, (NMC111)^{2+}$) even though the same concentration of $TMSO_4$ is used for precipitating their carbonates, there can be two possible reasons that could lead to different magnitude of SSR for each of these precipitates:

a) Different $TMCO_3$ demonstrates different magnitudes of solubility product.

$$K_{SP,MnCO_3} \neq K_{SP,NiCO_3} \neq K_{SP,CoCO_3} \neq K_{SP,NMC111CO_3} \quad (14)$$

b) Different transition metals (TM^{2+}) react with the other ions or species present in the solution (NH_4^+, OH^-, NH_3) in different ways.

Accordingly, even with the same concentration of $TMSO_4$ and NH_4HCO_3 reactants, it is possible to obtain different SSR as the type of transition metal is varied. The exact concentration of available TM^{2+} cations and CO_3^{2-} anions is obtained by solving the mass balance equations provided in Eqs. (1) – (5) in the Methodology section and the equilibrium relations provided in Table S1.

Supersaturation ratio experienced by the four different types of $TMCO_3$ with increasing amount of NH_4HCO_3 concentration is demonstrated in Figure 3. Concentration of NH_4HCO_3 in the solution is dictated by the ammonia over transition metal ratio ($[NH_4^+]/[TM^{2+}]$), which is shown along the x-axis in Figure 3. Following earlier research activities,[41, 49] the $[NH_4^+]/[TM^{2+}]$ ratio is varied between 1.0 and 40.0 to estimate the optimum amount of NH_4HCO_3 that leads to the maximum magnitude of SSR for all the individual $TMCO_3$. Both the $TMSO_4$ and NH_4HCO_3 completely dissociates into the respective cations and anions after dissolving in water, the reactant solution in this case, according to the following relations:

$$TMSO_4 \rightleftharpoons TM^{2+} + SO_4^{2-} \quad \text{and} \quad NH_4HCO_3 \rightleftharpoons NH_4^+ + HCO_3^- \quad (15)$$

Some of the TM^{2+} cations get consumed by the metal ammonia complex ($[TM(NH_3)_n]^{2+}$), the relations for which are depicted in Table S1. Similarly, not all the bicarbonate anions (HCO_3^-)

dissociate into carbonates (CO_3^{2-}), and extent of this dissociation depends on the presence of other reactants as well as the pH of the reacting solution (relevant equilibrium constants are provided in Table S1 in the Supporting Information (SI) section). The free TM^{2+} are available to react with the CO_3^{2-}, as shown in Eq. (8), which leads to the formation of the $TMCO_3$ precipitates. Increasing the concentration of NH_4HCO_3 leads to an increase in the concentration of available CO_3^{2-}, which effectively leads to an increase in SSR even though the concentration of TM^{2+} remains almost constant. As a result, with increasing $[NH_4^+]/[TM^{2+}]$ ratio, the SSR for $MnCO_3$, $CoCO_3$, and $NMC111CO_3$ increases, which is clearly depicted in Figure 3 by the red, blue, and magenta lines, respectively. The variation in the magnitude of SSR for the different $TMCO_3$ can be attributed to the difference in their solubility products, for example, $MnCO_3$ demonstrates the lowest solubility product, which leads to the highest SSR (denoted by the red circles).[28, 61]

The supersaturation ratio for $NiCO_3$ is denoted by the black squares in Figure 3, which is substantially smaller than the other three $TMCO_3$. This can be attributed to the relatively larger magnitude of $K_{SP,NiCO_3}$ as compared to the solubility product of other $TMCO_3$ (see Table S1 for the exact numbers).[28] Also, the SSR for $NiCO_3$ does not demonstrate a monotonic trend with the $[NH_4^+]/[TM^{2+}]$ ratio, and shows a maximum at around 15 – 20 ($[NH_4^+]/[TM^{2+}] \sim 15-20$). It has been explained in the previous paragraph that increasing the concentration of NH_4HCO_3 (or $[NH_4^+]/[TM^{2+}]$ ratio) leads to an increase in the concentration of available CO_3^{2-} anions that can react with Ni^{2+} to form $NiCO_3$. This explains the increase in SSR of $NiCO_3$ with increasing $[NH_4^+]/[TM^{2+}]$ ratio, which is observed only for $[NH_4^+]/[TM^{2+}]$ smaller than 10 ($[NH_4^+]/[TM^{2+}] < 10$). The decrease in SSR of $NiCO_3$ for $[NH_4^+]/[TM^{2+}] > 20$ can only be explained by a decrease in the available amount of free Ni^{2+} cations observed with increasing ammonia concentration. This observation is in line with the enhanced formation of nickel ammonia

complex ($[Ni(NH_3)_n]^{2+}$) with increasing concentration of the NH_4^+ ions within the solution.[59] Consumption of a substantial amount of the nickel cations in the form of nickel ammonia complex can decrease the concentration of available Ni^{2+} that can react with the CO_3^{2-} to form the $NiCO_3$ precipitate. Hence, with increasing $[NH_4^+]/[TM^{2+}]$ ratio, the SSR for $NiCO_3$ decreases.

Following this analysis, for precipitating $MnCO_3$, $CoCO_3$, and $NMC111CO_3$, the $[NH_4^+]/[TM^{2+}]$ ratio is maintained constant at 40, which leads to the maximum magnitude of SSR. However, for precipitating $NiCO_3$, the $[NH_4^+]/[Ni^{2+}]$ ratio is maintained at 15 that leads to the largest magnitude of SSR. The exact magnitude of $[NH_4^+]/[TM^{2+}]$ where the precipitation of the various $TMCO_3$ is conducted, is also highlighted in Figure 3 by greenish shades.

Chemical composition of precipitates and corresponding reaction mechanism: Relative amount of different transition metals within the precipitate is measured using the EDX mapping technique (as mentioned in the Methodology section). This technique is not considered quantitative, and the results are included here only as an estimation.[77] As expected, for $MnCO_3$, $CoCO_3$, and $NiCO_3$, the only transition metal present within the precipitate is Mn, Co, and Ni, respectively. For $NMC111CO_3$ precipitates (SEM image shown in Figure 4(a)), the desired chemical composition is equal amount of Mn, Co, and Ni, which should result in 33.33% of each of the transition metals. The elemental distribution of Mn, Co, and Ni, within the precipitated $NMC111CO_3$ is demonstrated in Figure 4(b), 4(c) and 4(d), and their mass and atomic distribution is tabulated in Figure 4(e). It is evident that the precipitates appear to be rich in Mn (content more than 50%), and the relative amount of Ni in the precipitate is much less than expected, only ~10%. Note that the initial transition metal solution contained equal amount $(1.5\ mM)$ of each of the $TMSO_4$, and the $[NH_4^+]/[TM^{2+}]$ ratio is maintained at 15 and 40, in two different precipitation experiments. Note that the distribution of Mn, Co, and Ni is uniform throughout the precipitate,

which negates the possibility of inhomogeneous precipitation of $TMCO_3$. X-ray diffraction study conducted on the sample with $[NH_4^+]/[TM^{2+}]$ ratio kept constant at 15 confirms the formation of the expected $TMCO_3$ precipitate (see Figure 5(g)). Precipitation of less Ni and more Mn in the final $NMC111CO_3$ precipitate is explored further in the subsequent paragraphs. Note that powder X-ray diffraction shows that the pure Co and Ni precipitates are not primarily the expected carbonates (Figures 5(e) and 5(f)); rather, most likely also contains metal hydroxide species as impurities.[45]

Distribution of various ions within the reacting solution is estimated by solving the mass balance and equilibrium relations provided in Eqs. (1) – (5) and Table S1 (in SI), respectively. According to the existing literature, formation of the $TMCO_3$ precipitate can occur through two different mechanisms:

a) Reaction I: The first possibility is reaction between transition metal ammonia complex ($[TM(NH_3)_n]^{2+}$) with the CO_3^{2-} anions that leads to precipitation of $TMCO_3$ and release of ammonia to the solution (see Eq. (8) for details).[64]
b) Reaction II: The second one is direct reaction of the transition metal cations (TM^{2+}) with the carbonate anions (CO_3^{2-}) that leads to the precipitation of $TMCO_3$ (see Eq. (9)).[28]

A third possible mechanism is a combination of these two reactions, which will also be briefly discussed below.

Extent of the $TMCO_3$ precipitates as a function of the $[NH_4^+]/[TM^{2+}]$ ratio, as predicted by the reaction I, is denoted by the dashed lines in Figure 4(f), where black indicates Ni, blue denotes Co, and red lines stand for Mn. According to reaction I, to precipitate any amount of $TMCO_3$ it needs to form the metal ammonia complex first and increasing the concentration of $[NH_4^+]$ should result in the formation of enhanced amount of the metal ammonia complex. For smaller magnitudes of $[NH_4^+]/[TM^{2+}]$, majority of the metal ammonia complex is formed with

Ni^{2+} ($[Ni(NH_3)_n]^{2+}$), and very small amount of Mn^{2+} complex with ammonia to form $[Mn(NH_3)_n]^{2+}$. Accordingly, at small $[NH_4^+]/[TM^{2+}]$ ratio, reaction I predicts enhanced precipitation of $NiCO_3$, and small amount of $MnCO_3$ should precipitate. However, with increasing $[NH_4^+]/[TM^{2+}]$ ratio, enhanced amount of $[Mn(NH_3)_n]^{2+}$ and $[Co(NH_3)_n]^{2+}$ is formed (along with $[Ni(NH_3)_n]^{2+}$), which leads to an increase in $MnCO_3$ and $CoCO_3$ in the final precipitate (along with $NiCO_3$). As a result, with increasing $[NH_4^+]/[TM^{2+}]$ ratio, the relative amount of Ni in the final precipitate decreases, while relative amount of Mn and Co increases. Note that even with $[NH_4^+]/[TM^{2+}] \sim 40$, reaction I predicts that the precipitates should be rich in Ni, which does not agree with the experimental observation, where Ni deficient precipitates are formed (see Figure 4(e)).

Under the assumption that reaction II, where the TM^{2+} cations directly react with the CO_3^{2-} anions, is the dominant mechanism for the precipitation of $TMCO_3$, the relative amount of Mn, Co, and Ni, in the $NMC111CO_3$ precipitate is shown in Figure 4(f) by the red, blue, and black solid lines, respectively. It is evident from the figure that with increasing $[NH_4^+]/[TM^{2+}]$ ratio, the amount of Ni in the precipitate decreases, amount of Mn increases, and the concentration of Co remains almost constant. Increasing concentration of $[NH_4^+]$ in the reacting solution leads to an enhancement in the formation of transition metal ammonia complex ($[TM(NH_3)_n]^{2+}$), which effectively decreases the concentration of available cations that can react with CO_3^{2-} anions to form the $TMCO_3$ precipitate. Among the three different transition metals, Ni forms the strongest $[Ni(NH_3)_n]^{2+}$ with increasing $[NH_4^+]$, which consumes large amount of Ni^{2+} cations from the solution, and the concentration of Ni participating in its precipitation decreases dramatically. On the contrary, Mn does not form a strong $[Mn(NH_3)_n]^{2+}$ even with increasing concentration of $[NH_4^+]$, and finally the relative amount of Mn in the final $NMC111CO_3$ precipitate increases (red

solid line in Figure 4(f)). Interestingly, the relative amount of Co in the precipitate does not change substantially with increasing amount of $[NH_4^+]$ and remains very close to the desired 33.33%. Following this particular analysis, it is possible to precipitate equal amount of Mn, Co, and Ni in the $NMC111CO_3$ precipitate if smaller magnitudes of the $[NH_4^+]/[TM^{2+}]$ ratio is used ($[NH_4^+]/[TM^{2+}] \sim 1$).

For $[NH_4^+]/[TM^{2+}] \sim 40$, the total amount of Mn in the $NMC111CO_3$ precipitate is much larger than Ni and Co, and the concentration of Ni in the precipitate is much less than 10%, which is consistent with that observed in the experiments (see the Table in Figure 4(e)). The experimentally observed relative concentrations of Mn, Co, and Ni in the $NMC111CO_3$ precipitate obtained with $[NH_4^+]/[TM^{2+}] \sim 40$ and $[NH_4^+]/[TM^{2+}] \sim 15$ is denoted in Figure 4(f) by the red circles, blue diamonds, and black squares, respectively. It is evident that the experimentally observed fraction of the three transition metals closely follow the predictions obtained by considering precipitation of $TMCO_3$ through direct reaction between the TM^{2+} cations and CO_3^{2-} anions, or the reaction II denoted by the solid lines in Figure 4(f). Hence, it can be concluded that even when a mixture of the transition metals is present within the reactor, individual transition metals react separately with the CO_3^{2-} anions while forming the $TMCO_3$ precipitate. Reaction between the $[TM(NH_3)_n]^{2+}$ cations and CO_3^{2-} anions can be neglected altogether, which is a significant deviation from the present understanding of the coprecipitation reaction mechanism.

It is worth mentioning that a third possibility is simultaneous occurrence of reactions I and II during precipitating the $TMCO_3$. Under this scenario, almost equal amount of Mn, Ni, and Co should have precipitated in the final $NMC111CO_3$, because the transition metal cations can exist either as free ions floating in the solution (TM^{2+}), or in the form of metal ammonia complex ($[TM(NH_3)_n]^{2+}$). If both of them react with CO_3^{2-} anions, almost similar amount of precipitates

is expected to occur. The final fraction of transition metal in the precipitate might vary slightly due to the difference in the solubility product of the different $TMCO_3$ (see Eq. (14)), but the variation is expected to be minimal. However, comparison with the experimental results reveals that Mn-rich and Ni-deficient precipitates are formed, which does not correlate with the predictions obtained from the combined occurrence of reactions I and II. Accordingly, in the present study, precipitation of $TMCO_3$ will be considered to occur only thorough the direct reaction between TM^{2+} cations and CO_3^{2-} anions, or the reaction II.[28, 60]

Morphology of the precipitated primary particles and the primary particle aggregates: After precipitating the $MnCO_3$, $CoCO_3$, $NiCO_3$, and $NMC111CO_3$ from a 4.5 mM solution of $TMSO_4$, morphology of their primary particles is investigated using the transmission electron microscopy (TEM) techniques. Note that the $[NH_4^+]/[TM^{2+}]$ ratio is maintained at 40 for precipitating $MnCO_3$, $CoCO_3$, and $NMC111CO_3$, whereas a ratio of 15 is used for $NiCO_3$ formation in order to maximize the supersaturation ratio during the precipitation of the respective $TMCO_3$ (see Figure 3 for more details). The TEM images of the $TMCO_3$ primary particles, shown in Figures 5(a) – 5(d), reveal that $MnCO_3$ demonstrates a faceted single crystalline, or pseudo single crystalline, morphology with particle size in the range of several hundreds of nanometers (see Figure 5(a)).[41] Figure 5(b) demonstrates that the primary $CoCO_3$ particles exist as rough aggregates, which can form either through surface nucleation and growth, or due to agglomeration of multiple small sized nuclei. The sizes of these $CoCO_3$ primary particles are in the range of 3 – 5 nm. The $NiCO_3$ primary aggregates are shown in Figure 5(c), which appear to be smoother than $CoCO_3$, with size of primary particles ranging between 1 – 2 nm. Primary particle sizes for the $NiCO_3$ and $CoCO_3$ is extracted from the full width half maximum (FWHM) of the corresponding XRD peaks, as provided in Figures 5(e) and 5(f) (also tabulated in Figure 5(i)). The XRD peaks

of the Ni and Co precipitates (shown in Figures 5(e) and 5(f)) also reveals that the precipitates are not pure phase carbonates, rather a mixture of transition metal carbonates and hydroxides. Finally, Figure 5(d) depicts the morphology of the $NMC111CO_3$ primary particles, which are approximately 10 – 20 nm in size, spherical in shape, and exist in the form of rough aggregates. The XRD pattern of the $NMC111CO_3$ (shown in Figure 5(g)) demonstrates strong resemblance to $MnCO_3$ due to their highly correlated peaks. This similarity alludes to the possibility of the formation of $MnCO_3$ nuclei and subsequent precipitation of all transition metals on top of it, which leads to the final $NMC111CO_3$ precipitates with a structure similar to the $MnCO_3$ one. The similarities between the primary particle morphology of $NMC111CO_3$ and $CoCO_3$, in terms of their rough appearance, are worth noting, which is a major deviation from the smooth appearance of the $NiCO_3$ precipitates. Also, note that except $MnCO_3$, none of the $TMCO_3$ primary particles demonstrate faceted structure, and rather prefers an irregular, or spherical shape.

In order to decipher the different primary particle morphologies for $MnCO_3$, $CoCO_3$, and $NiCO_3$, atomic scale simulations using the density functional theory (DFT) are conducted. The minimum energy surfaces of the three different transition metal carbonates ($MnCO_3$, $CoCO_3$, and $NiCO_3$) are estimated and their minimum energy Wulff configuration is determined. According to the DFT calculations, for all the three $TMCO_3$, the minimum energy surface is the (102) facet. The magnitude of the minimum surface energy is $1.05\ J/m^2$, $1.53\ J/m^2$, and $1.79\ J/m^2$ for $MnCO_3$, $CoCO_3$, and $NiCO_3$, respectively, which is tabulated in Figure 5(h) (please refer to Table S4 in the Supplementary Information section for a comparison of surface energies predicted by DFT). Since, the (102) surface leads to a rhombohedral shaped minimum energy Wulff construction,[41] all the three $TMCO_3$ should demonstrate rhombohedral shaped faceted particles. However, the TEM images clearly reveal that only the $MnCO_3$ demonstrates a faceted primary

particle morphology. All the other transition metal carbonates ($CoCO_3$, $NiCO_3$, and $NMC111CO_3$) depict spherical or irregular shaped primary particles. Inability of the Ni and Co containing precipitates to form the minimum energy configuration (thermodynamically equilibrium particle shape) can possibly be attributed to their limited growth kinetics, or to the precipitation of transition metal hydroxide impurities (see XRD peaks in Figures 5(e) and 5(f)), which eventually leads to the formation of the spherical or irregular shaped primary particles.

TEM images of the various $TMCO_3$ primary particles shown in Figures 5(a) – 5(d) clearly indicate that only $MnCO_3$ demonstrates larger sized primaries, in the range of hundreds of nanometers. Other Ni and Co containing precipitates ($CoCO_3$, $NiCO_3$, and $NMC111CO_3$) demonstrate much smaller primary particles, with size ranging between a few nanometers (1 – 2 nm for $NiCO_3$) to tens of nanometers (10 – 20 nm for $NMC111CO_3$), which is also tabulated in Figure 5(i). Size of the primary particles is determined by their rate of growth, which depends on the supersaturation ratio (SSR) as well as the reaction rate constant. It is evident from Figure 3 that the SSR experienced by $MnCO_3$ is largest, around 10^6, whereas the SSR experienced by $CoCO_3$ and $NMC111CO_3$ is around 10^4. $NiCO_3$ experiences the lowest magnitude of SSR, which is around 10. Due to the large variation in SSR experienced by the Ni and Co containing precipitates, the trend in primary particle size cannot be explained simply through the difference in their SSR. The difference in reaction rate constant associated with the direct precipitation process $\left(k_{\mathrm{pp}}\right)$ needs to be invoked to decipher the variation in primary particle size experienced by $MnCO_3$ versus the Ni and Co containing precipitates. It is argued that the reaction rate constant experienced by $MnCO_3$ is orders of magnitude larger than the reaction rate constants for Ni and Co containing precipitates $\left(k_{\mathrm{pp,MnCO_3}} > k_{\mathrm{pp,NiCO_3}} \sim k_{\mathrm{pp,CoCO_3}} \sim k_{\mathrm{pp,NMC111CO_3}}\right)$. This claim is supported by the $k_{\mathrm{pp,MnCO_3}} \sim 10^{-4}\,\mathrm{m/s}$, as reported in Garcia et al,[41] which is around two to three orders of

magnitude larger than the $k_{\mathrm{pp}}{\sim}10^{-7}\ \mathrm{m/s}$ for Ni and Co containing carbonates (as mentioned in Table S2 in the SI section). Smaller reaction rate constants for Ni and Co containing precipitates can be attributed to the orders of magnitude slower water exchange rate constants experienced by the Ni^{2+} and Co^{2+} aqua ions, as compared to their Mn^{2+} counterpart.[48] Also, the presence of $TM(OH)_2$ and TMOOH based impurities within the $NiCO_3$ and $CoCO_3$ precipitates tends to slow down their rates of precipitation as well as their surface diffusivities (see Figure 5(e) and 5(f)).[45]

A combination of faster reaction rate constant and higher magnitudes of SSR leads to larger growth rate for the $MnCO_3$ precipitates, around $10^4\ \mu\mathrm{m/min}$, which is demarcated by the red filled square along the x-axis in Figure 6. On the other hand, the smaller reaction rate constants for the Ni and Co containing precipitates lead to smaller values of growth rates, around $5\ \mu\mathrm{m/min}$ to $20\ \mu\mathrm{m/min}$, which are also provided in Figure 6 by the black, blue, and magenta filled circles. This larger growth rate of $MnCO_3$ and smaller rates experienced by the $NiCO_3$, $CoCO_3$, and $NMC111CO_3$, successfully explains the larger sub-micron sized primary particles of $MnCO_3$, and nanometer sized primaries for Ni and Co containing carbonates. Note that the growth rate of the $TMCO_3$ particles is less dependent on the corresponding SSR, and depends more on the individual reaction rate constant.

The tendency for agglomeration, or growth through surface nucleation, is dictated by the overall surface energy of the primary particles, which is estimated using Eq. (S15) (provided in the Supporting Information section). The total surface energy is directly proportional to the surface energy density (γ) and inversely proportional to the size of the primary particle of the precipitates.[42] As a result, smaller particles demonstrate higher surface energies and prefer to form aggregates in order to minimize the overall energy of the system. As provided in Figure 5(e), the surface energy density of the Ni and Co containing precipitates $\left(\gamma_{\mathrm{NiCO_3}}, \gamma_{\mathrm{CoCO_3}}\right)$ is larger than

$MnCO_3$ (γ_{MnCO_3}), which can also be written as $\gamma_{MnCO_3} < \gamma_{NiCO_3} < \gamma_{CoCO_3}$. This indicates that due to a combination of smaller growth rate as well as larger surface energy densities, the Ni and Co containing carbonates should demonstrate larger overall surface energies and higher tendency of agglomeration, as compared to $MnCO_3$. Note that the magnitude of the surface energy densities between $CoCO_3$ and $MnCO_3$ varies by only a factor of two $\left(\left(\gamma_{CoCO_3}/\gamma_{MnCO_3}\right)\sim 2\right)$, whereas the growth rate of the Mn containing versus Ni or Co containing precipitates differ by several orders of magnitude (see Figure 6 along the x-axis).

In conclusion, the tendency to form aggregates, or grow through the surface nucleation phenomena, which is dictated by the surface energy of the precipitates, differs substantially between $MnCO_3$, $NiCO_3$, $CoCO_3$, and $NMC111CO_3$. The surface energy experienced by the various precipitates is depicted along the y-axis in Figure 6. Due to its faster growth rate $MnCO_3$ experience much less surface energy, and the particles demonstrate much less surface growth.[49] On the other hand, Ni and Co containing precipitates encounter smaller growth rates and much higher magnitudes of surface energy, which leads to aggregation of primary particles or growth through surface nucleation phenomena, both of which helps to minimize the overall energy of the precipitates.[64] This explains the enhanced amount of surface nucleation and growth observed in the Ni and Co containing carbonate primary particles (see the TEM images shown in Figures 5(b) – 5(d)).

It is evident from Figures 3, 5, and 6, that for $NiCO_3$, $CoCO_3$, and $NMC111CO_3$ precipitates, in spite of the variation in their supersaturation ratios (SSR) (different SSR shown in Figure 3), demonstrate growth through surface nucleation and aggregation process, which can be attributed to the limited reaction rate constant experienced by these Ni and Co containing transition metal carbonates. However, there exist subtle differences in their primary particle morphologies, which

is evident from the TEM images shown in Figures 5(b) – 5(d), as well as pointed out in Figures 7(b) – 7(d). $CoCO_3$ and $NMC111CO_3$ experience higher magnitudes of supersaturation ratio ($SSR{\sim}10^4$) and the surface of the aggregates of the primary particles appears to be rough, which is clearly shown in Figures 7(b) and 7(d). On the other hand, Figure 7(c) depicts that $NiCO_3$ demonstrates a relatively smooth surface of the primary aggregates, which is accompanied with much lower magnitudes of the supersaturation ratio ($SSR{\sim}10$). Appearance of the smooth or rough surface of the primary aggregates impacts the active surface area of the primary particles exposed for reaction with oxygen and lithium salt during the calcination process.[39] Hence, it is important to understand why certain precipitates demonstrate a smooth surface (such as, $NiCO_3$), whereas the others show rough surface morphologies (for example, $CoCO_3$, $NMC111CO_3$).

In order to elucidate the difference in primary aggregate surface morphologies demonstrated by $NiCO_3$, $CoCO_3$, and $NMC111CO_3$, it is very important to understand the reaction mechanism, and various driving forces, that govern the overall precipitation process. It has already been argued in Figure 6 that due to their limited reaction rate constants, the Ni and Co containing precipitates prefer to grow through the surface nucleation and agglomeration processes, which will be characterized as surface growth phenomena in the following paragraphs. There exist two major driving forces that dictate the morphology of the primary particle aggregates as provided below (also schematically demonstrated in Figure 7(a)):[42]

a) Driving force for precipitation reaction, which is controlled by the magnitude of the supersaturation ratio (SSR), where large SSR prefers precipitation and surface growth at higher rates.
b) Driving force for surface energy minimization, which occurs through the diffusion of transition metal cations (TM^{2+}) and carbonate anions (CO_3^{2-}) within the reacting solution, and helps to

form the next surface nucleus at a location that minimizes surface energy. Note that faster diffusion of reactants within the solution should result in smooth surface of the primary particle aggregates.

Accordingly, a Monte-Carlo based computational technique is developed to decipher the competition between the driving forces for precipitation and surface energy minimization in determining the final morphology of the primary aggregates. Details of the computational methodology involve minimization of surface energy $\left(\min\left(E_{\mathrm{surf,tot}}\right)\right)$, diffusion of transition metals (diffusion coefficient given as D_{TM}), formation of new surface nuclei (rate coefficient given as k_{sn}), and supersaturation ratio of the reactants (SSR), all of which are provided in Eqs. (10) – (13) as shown in the Methodology section. The parameter used in this analysis is provided in Table S2 in the Supporting Information (SI) document.

Detailed simulation of the precipitation of Ni and Co containing transition metal carbonates through the surface growth phenomena is conducted, and the predicted primary particle morphologies are demonstrated in Figures 7(e) – 7(g). Due to its higher supersaturation ratio $(\mathrm{SSR}{\sim}10^4)$, rate of precipitation experienced by $\mathrm{CoCO_3}$ is very high, which leads to quick surface growth phenomena without allowing much time for the surface energy minimization. Hence, an extremely rough surface of the primary aggregates is observed for $\mathrm{CoCO_3}$, which is shown in Figure 7(e) that correlates well with the experimental observation depicted in Figure 7(b). Lower supersaturation ratio of $\mathrm{NiCO_3}$ $(\mathrm{SSR}{\sim}10)$ leads to slower surface nucleation and surface growth process, which provides sufficient time for the diffusion of transition metals to find locations for surface nucleation that minimizes the overall surface energy of the precipitates. As a result, relatively smooth surface of the $\mathrm{NiCO_3}$ precipitate is predicted in Figure 7(f), which agrees well with the primary particle morphology depicted by the TEM images in Figure 7(c). Finally, the

$NMC111CO_3$ also experiences higher magnitudes of supersaturation ratio ($SSR \sim 10^4$), which is very similar to the $CoCO_3$ precipitates, where the driving force for precipitation dominates over the surface energy minimization mechanism. As a result, the final primary particle aggregates of $NMC111CO_3$ demonstrate a rough surface morphology as depicted in Figure 7(g), which also shows good agreement with the rough surface patterns depicted by the TEM images in Figure 7(d). Hence, the competition between the rate of precipitation and diffusion of transition metal is capable of successfully capturing the variation in the morphology of the primary aggregate for the various Ni and Co containing transition metal carbonate precipitates.

Computational simulation of time evolution of the secondary particle morphology: Understanding the evolution of the morphology of the secondary particles during the coprecipitation process is of major significance.[43] The size and size distributions of these secondary particles obtained from coprecipitation remain almost constant even after the calcination of the cathode particles, which demonstrates substantial influence on the overall cell performance. In a realistic transition metal carbonate cathode precursor, a combination of Ni, Mn, and Co is usually precipitated (such as, $NMC111CO_3$, $NMC352CO_3$, etc.),[16, 64] and precipitation of individual $TMCO_3$'s ($NiCO_3, MnCO_3, CoCO_3$) are considered as model systems, mostly for academic interest. Accordingly, in order to provide a better understanding of the impact of a combination of different transition metals (Ni, Mn, Co) on the evolution of the overall $TMCO_3$ secondary particles, precipitation, and subsequent particle morphology evolution of $NMC111CO_3$ is investigated here.

Experimentally, $NMC111CO_3$ is precipitated using a batch reactor with two different concentrations of the total transition metal sulfate, 4.5 mM and 45 mM, where the concentration of the individual $TMSO_4$ is about one third of the total transition metal concentration. The

precipitates are extracted after running the reaction for 30 minutes, and the morphology of the secondary particles are characterized using benchtop scanning electron microscopes (SEMs). SEM images of the secondary particles obtained for total transition metal concentrations of 4.5 mM and 45 mM are shown in Figures S1(a) and S1(b), which appears to demonstrate secondary particle sizes around 4.25 μm and 5.5 μm, respectively. Enhanced concentrations of $TMSO_4$ lead to higher supersaturation ratios of reactants within the solution. Increase in secondary particle size under higher transition metal concentrations can be attributed to the formation of more nuclei at higher supersaturation ratios, and their agglomeration, which eventually leads to the formation of the enlarged secondary particles. This particular mechanism will be discussed in more detail in the subsequent paragraphs. Note that, even though equal moles of $NiSO_4$, $MnSO_4$, and $CoSO_4$ are dissolved within the reacting solution with an expectation of precipitating $NMC111CO_3$, the final precipitate actually turns out to contain less than desired Ni and more than expected amount of Mn (see Figure 4). This particular variation is attributed to the difference in solubility of $NiCO_3$, $MnCO_3$, and $CoCO_3$ in water, as well as the difference in their tendency to form the transition metal ammonia complex ($[TM(NH_3)_n]^{2+}$) (see the discussion associated with Figure 4 for more details).

In the present context, morphology of the secondary particles of $NMC111CO_3$ will be investigated without paying much attention to their chemical composition. It is evident from Figures 5, 6, and 7, that the primary particles of $NMC111CO_3$ are relatively small in size, in the range of 10 nm – 20 nm. It is also reported that the growth of the primary aggregates for $NMC111CO_3$ occurs through a surface nucleation mechanism, which leads to the formation of a rough surface. Because of the extremely small size of the primary particles, they are not modeled separately. Nucleation and growth of the primary aggregates, which evolve through the surface

growth phenomena, will be modeled instead. The following features are simulated to capture the growth of the secondary particles:[46, 78, 79]

1. Nucleation of the primary aggregates
2. Growth of the primary aggregates
3. Movement of the primary aggregates through diffusion or fluid flow induced convection
4. Agglomeration of the primary aggregates and formation of secondary particles

Details of the numerical techniques used for simulating these physicochemical phenomena are provided in Eqs. (S9) – (S16) within the Supplementary Information section.[80] Note that the growth of the primary aggregates occurs due to both direct precipitation as well as surface nucleation induced growth of the $TMCO_3$, which renders the growth rate of the primary particle aggregates to be larger than the direct precipitation induced growth rate of the primary particles (see Table S2 in SI). It is worth mentioning that the movement of the secondary particles is also considered in the present computational methodology. Couple of model parameters that influences the growth of the secondary particles are:

a) Velocity of the liquids that carries the particles around (v_{liq}) and dictates how quickly the particles see other particles (or agglomerates) that can lead to their agglomeration.
b) Reaction rate constant for the growth of the primary particle aggregates (k_{ref}), which is directly proportional to its growth rate.

Computationally predicted evolution in secondary particle size with time for the two different concentrations of the $TMSO_4$, namely 4.5 mM and 45 mM, is shown in Figure 8 by the black and red lines, respectively. The initial $[NH_4^+]/[TM^{2+}]$ ratio is maintained at 40 for the computational simulation, which is consistent with the experiments. The experimentally observed secondary particle sizes for $TMSO_4$ concentrations of 4.5 mM and 45 mM, obtained after precipitating for 30

minutes, are also pointed out in Figure 8 by the black and red circles, respectively. Good correlation between the experiments and model predictions is obtained for liquid velocity, $v_{liq} \sim 10^{-5}$ m/s, and reaction rate constant, $k_{ref} \sim 10^{-6}$ m/s, which is also pointed out in Figure 8. Larger secondary particle size with enhanced transition metal concertation can be attributed to the formation of larger number of nuclei at higher metal concentration and their agglomeration occurring over long time. Note that if agglomeration of particles is not considered, the particle sizes tend to decrease with increasing metal concentration because the increase in number of nuclei far exceeds the total amount of transition metal present within the solution.

Note that the velocity of the liquid that carries the particles around within the reacting solution may not be the same as the liquid velocity dictated by the stirring speed (around 500 rpm in the present experiments). This difference in liquid velocities can be attributed to the fact that the stirring speed controls the speed of the larger vortices or larger eddies that form inside the reactor.[81] However, the secondary particles being much smaller in size, ranging around a few microns, their movement is mostly controlled by the size and velocity of the smaller eddies, which can be orders of magnitude different from that observed for the larger eddies.[81] Accordingly, the liquid velocity (v_{liq}), along with the reaction rate constant (k_{ref}), are used as fitting parameters that provide good correlation with the experimentally observed secondary particle sizes. Evolution of secondary particle size, without considering any liquid velocity, but different magnitudes of the reaction rate constants, is shown in Figure S2(a). All the secondary particle sizes, irrespective of the reaction rate constant, significantly underpredict the experimentally observed secondary particle size at transition metal concentrations around 4.5 mM. It is evident that convective flow of liquid induced movement of particles is necessary for enabling agglomeration and creating secondary particles with size equivalent to the experimentally observed ones. Accordingly, Figure

S2(b) demonstrates the secondary particle size obtained for different liquid velocities while maintaining a fixed magnitude of the reaction rate constant ($k_{ref} \sim 10^{-6}\ m/s$). As evident from the figure, liquid velocity can substantially influence the secondary particle size through the agglomeration mechanism. A particular combination of $v_{liq} \sim 10^{-5}\ m/s$ and $k_{ref} \sim 10^{-6}\ m/s$ provides good correlation with experimentally observed particle size obtained at $TMSO_4$ concentrations of 4.5 mM, which is also shown in Figure 8.

In order to further verify the developed mathematical framework for estimating the $TMCO_3$ secondary particle sizes, the same model is run for two different cases, where in one $[NiSO_4]:[MnSO_4]$ is maintained at 50:50 and the other scenario uses $[NiSO_4]:[MnSO_4]$ to be around 90:10 (no cobalt is used in any of these two simulations). The total concentration of TM^{2+} is kept constant at 12 mM and ammonia over transition metal ratio of 15 $\left(([NH_4^+]/[TM^{2+}]) \sim 15\right)$ is maintained. Similar experiments were also run in the batch mode to understand the evolution of secondary particles in these conditions. The model predicted evolution of primary aggregates and secondary particles are shown in Figure S3(a), S3(b) and S3(c), whereas the experimental observations are demonstrated in Figure S3(d) and S3(e). Decreasing secondary particle size with increasing Ni-content is captured by the computational model, which is consistent with the experimental observations. Note that the reaction rate constant, k_{ref}, is assumed to be a function of Mn fraction, where for 50% and 10% manganese, the magnitude of k_{ref} decreases from $10^{-5}\ m/s$ to $10^{-7}\ m/s$.

After the calibration of the computational methodology for predicting the secondary particle sizes, it is worth investigating the influence of the transition metal concentration ($[TM^{2+}]$) and ammonia over metal ratio ($[NH_4^+]/TM^{2+}$) on the overall size and size distribution of the secondary particles. Multiple simulations are conducted by varying the transition metal

concentration from 1.5 mM to 22.5 mM, where the concentration of individual $NiSO_4$, $CoSO_4$, and $MnSO_4$ are maintained at one third of the total $TMSO_4$ concentration. The ammonia over metal ratio ($[NH_4^+]/[TM^{2+}]$) is also varied between 1.0 and 40.0 in the simulated cases. The computationally predicted average sizes of the secondary particles are shown in Figure 9 in the form of a phase map between the total metal concentration ($[TM^{2+}]$) and ammonia over metal ratio ($[NH_4^+]/[TM^{2+}]$). Yellow region indicates larger particles with size greater than 10μm, whereas the green domain indicates smaller particles, less than 5μm in size. It is evident that increasing the concentration of transition metal results in an increase in the mean particle size, which can be attributed to larger number of nuclei at higher concentrations, and their agglomeration leads to the formation of larger sized secondary particles.

On the other hand, impact of the ammonia over metal ratio is not as straightforward; for smaller $[TM^{2+}]$, increasing $[NH_4^+]/[TM^{2+}]$ leads to a slight increase in the secondary particle size. However, for larger magnitudes of $[TM^{2+}]$, increasing $[NH_4^+]/[TM^{2+}]$ renders initially an increase, and then a decrease in the secondary particle size. Note that the variation in ammonia over transition metal ratio is conducted by altering the amount of NH_4HCO_3 in the solution. Increase in $[NH_4^+]$ also indicates an enhancement in $[HCO_3^-]$, which results in a larger magnitude of the $[CO_3^{2-}]$. As the $[NH_4^+]/[TM^{2+}]$ increases, the concentration of carbonate anions ($[CO_3^{2-}]$) also increase, which effectively leads to an increase in the supersaturation ratio (SSR) and higher growth rates of the primary aggregates. As a result, moderate increase in $[NH_4^+]/[TM^{2+}]$ lead to larger secondary particle sizes. On the other hand, very high concentrations of $[NH_4^+]$ can lead to the excessive formation of transition metal ammonia complex ($[TM(NH_3)_n]^{2+}$), which can effectively lower the concentration of available TM^{2+} cations that can react with CO_3^{2-} anions to form $TMCO_3$. Hence, increasing $[NH_4^+]$ can lower the SSR of $TMCO_3$ within the reacting solution

by consuming TM^{2+} cations. Accordingly, very high magnitudes of $[NH_4^+]/[TM^{2+}]$, with higher values of $[TM^{2+}]$, leads to slower growth rate of the primary aggregates, and the secondary particle size also decreases. Note that with $[TM^{2+}]\sim 20\text{mM}$ and $[NH_4^+]/[TM^{2+}] \sim 20-40$, the secondary particle size remains around $10\mu\text{m}$, which can be categorized as a relatively large sized secondary particle.

After investigating how the average secondary particle size changed with metal and ammonia concentration, their influence on the particle size distribution is worth studying. The standard deviation of the particle size is used as the descriptor for the size distribution of the particles. Accordingly, the standard deviation of the computationally predicted secondary particles is estimated and overlayed on top of the phase map in Figure 9 by the cyan and magenta circles. Before plotting, the magnitude of the standard deviation is normalized with respect to the average particle size in order to eliminate any spurious effects. The magenta color indicates wide distribution of particle sizes, whereas the cyan indicates a narrow distribution. Note that all the particle sizes and size distributions are plotted after 1 hour. Very narrow size distributions are observed for smaller metal concentrations and ammonia over metal ratios ($[TM^{2+}]\sim 1.5\text{ mM}, \text{and } [NH_4^+]/[TM^{2+}] \sim 1$). On the other hand, the most wide size distributions are observed for $[TM^{2+}]\sim 22.5\text{ mM}$ and $[NH_4^+]/[TM^{2+}] \sim 5$, while increasing $[NH_4^+]/[TM^{2+}] \sim 40$ results in a decrease in the size distribution under the same $[TM^{2+}]\sim 22.5\text{ mM}$.

Nucleation of new particles leads to an increase in standard deviation, whereas decrease in size distributions occurs through the Ostwald ripening mechanism.[46] With increasing metal concentration, the direct precipitation from solution tends to continue for longer times, which renders less time for the Ostwald ripening mechanism to minimize the size distribution. Hence,

increasing the concentration of transition metals leads to an increase in particle size distribution. Altering the ammonia over metal ratio also influences the SSR, rate of precipitation, and nucleation density, which affect the time for direct precipitation from reacting solution and Ostwald ripening induced growth of the secondary particles. In the present context, using $[TM^{2+}]\sim 22.5$ mM and $[NH_4^+]/[TM^{2+}] \sim 40$ provides quick precipitation and longer time for the growth of particles through the Ostwald ripening phenomena, which effectively helps to lower the particle size distribution.

Conclusion

Precipitation of transition metal carbonate $\left(Ni_xMn_yCo_zCO_3, \text{where}, x+y+z=1\right)$ cathode precursors is investigated using a combination of experimentation and computational methods. End members of the mixed transition metal carbonate cathode precursor, such as, $NiCO_3$, $MnCO_3$, and $CoCO_3$, are precipitated, along with equal amount of the three transition metals $NMC111CO_3$, in a batch reactor.[49] Analysis is conducted in batch mode to decipher the influence of thermodynamics and kinetics of the reactants on the evolution of particle morphology, without the unnecessary complications associated with the rates of reactant addition observed in CSTR type continuous systems. NH_4HCO_3 is used as the source of the carbonate anions within the reactor.[41, 49] Solubility of different transition metal carbonates in water differ over several orders of magnitude, which leads to a wide range of supersaturation ratios encountered during the precipitation of $NiCO_3$, $MnCO_3$, $CoCO_3$, and $NMC111CO_3$.[28, 59, 60]

Elemental composition of the final precipitates is determined using EDX mapping. Even though equal amounts of Ni, Mn, and Co salt is added to the reacting solution for precipitating $NMC111CO_3$ precursors, the final precipitates are always found to be Ni deficient. Computational

methodologies are developed considering the thermodynamic equilibrium between the various species within the reactor, which helps to decipher the elemental distribution of various transition metals in the cathode precursors.[59] Enhanced formation of the nickel ammonia complex reduces the concentration of freely available Ni^{2+} cations in the solution, which leads to less precipitation of Ni resulting in Ni deficient cathode precursors. During the precipitation of $NiCO_3$ and $CoCO_3$, it is possible to have hydroxide based impurity phases being precipitated out of the solution along with the desired carbonates, which can substantially influence the particle formation mechanism.

Morphology of the primary and secondary particles of the final precipitates is extracted using TEM and SEM imaging techniques, respectively. Computational methodologies are developed that successfully captures the competition between rate of precipitation and propensity for aggregation in determining the most efficient mechanism for surface energy minimization, which finally dictates the morphology of the precursor particles.[42] Higher reaction rate constants are preferrable for generating larger primary particles; whereas smaller reaction rate constant is necessary for the formation of aggregated secondary particles. Total concentration of transition metal and ammonia within the reacting solution controls the size and size distribution of the secondary particles to a large extent by altering the supersaturation ratio. Understandings developed from this analysis can help to precipitate cathode precursors with smaller primaries, which is expected to be good for calcination. Reaction conditions needed to precipitate small as well as large secondary particles, with a narrow size distribution, which can help to achieve higher energy density in next generation LIBs, can be estimated using the developed computational methodology.

Author Contributions

P.B. developed computational models, ran the simulations, generated figures, prepared the first draft; X.W. ran the precipitation experiments and generated data, revised the manuscript; M. W. conducted the XRD/EDX mapping, took high resolution SEM and TEM images, generated figures, revised manuscript; J. C. helped in running the experiments and generating the data; A. G. ran experiments, generated samples for further characterization, provided data for validating the computational models; J. C. G. ran atomistic simulations, generated figures; J. W. helped with collecting the high resolution SEM and TEM images, generated figures, revised manuscript; T. K. helped with XRD analysis and EDX mapping of the precipitated samples, revised manuscript; T. T. F. helped with the XRD, SEM and EDX of the precipitated samples, revised manuscript; H. I. ran atomistic simulations, conceived idea, revised manuscript; V. S. conceived the idea, helped with physical understanding of the processes involved, major revision of the manuscript, brought funding to conduct the research.

Conflict of Interest

The authors have no conflicts of interest to declare.

Acknowledgements

This research is supported by the Vehicle Technologies Office (VTO), Department of Energy (DOE), USA. Argonne National Laboratory is operated for DOE Office of Science by UChicago Argonne, LLC under the contract number DE- AC02-06CH11357. Work performed at the Center for Nanoscale Materials, a U.S. Department of Energy Office of Science User Facility, was supported by the U.S. DOE, Office of Basic Energy Sciences, under Contract No. DE-AC02-06CH11357. This research also used resources of the Advanced Photon Source, a U.S. Department

of Energy (DOE) Office of Science User Facility, operated for the DOE Office of Science by Argonne National Laboratory under Contract No. DE-AC02-06CH11357. The mail-in program at Beamline 17-BM contributed to the data. The authors also acknowledge the computing resources provided by the Laboratory Computing Resource Center (LCRC) at Argonne National Laboratory.

References

1. Janek, J. and W.G. Zeier, *Challenges in speeding up solid-state battery development.* Nature Energy, 2023. **8**(3): p. 230-240.
2. Manthiram, A., *A reflection on lithium-ion battery cathode chemistry.* Nature communications, 2020. **11**(1): p. 1550.
3. Meng, Y.S., V. Srinivasan, and K. Xu, *Designing better electrolytes.* Science, 2022. **378**(6624): p. eabq3750.
4. van den Brink, S., et al., *Identifying supply risks by mapping the cobalt supply chain.* Resources Conservation and Recycling, 2020. **156**.
5. Kim, Y., W.M. Seong, and A. Manthiram, *Cobalt-free, high-nickel layered oxide cathodes for lithium-ion batteries: Progress, challenges, and perspectives.* Energy Storage Materials, 2021. **34**: p. 250-259.
6. Li, W., E.M. Erickson, and A. Manthiram, *High-nickel layered oxide cathodes for lithium-based automotive batteries.* Nature Energy, 2020. **5**(1): p. 26-34.
7. Guo, W., et al., *In situ surface engineering enables high interface stability and rapid reaction kinetics for Ni-rich cathodes.* eScience, 2023. **3**(1): p. 100082.
8. Company, M. *Battery 2030: Resilient, sustainable, and circular*. 2023; Available from: https://www.mckinsey.com/industries/automotive-and-assembly/our-insights/battery-2030-resilient-sustainable-and-circular#/.
9. Sebrell, N. and F.V. Ivanov. *Nickel: Supply Risks and ESG Issues*. 2023 [cited 2023; Available from: https://insights.issgovernance.com/posts/nickel-supply-risks-and-esg-issues/.
10. Ramasubramanian, B., et al., *Recent development in carbon-LiFePO4 cathodes for lithium-ion batteries: a mini review.* Batteries, 2022. **8**(10): p. 133.
11. Guo, Y., et al., *Rejuvenating LiNi0. 5Co0. 2Mn0. 3O2 cathode directly from battery scraps.* EScience, 2023. **3**(2): p. 100091.
12. Holland, A. *Volkswagen's Long-term, High-Manganese Cathode Strategy*. 2021; Available from: https://www.idtechex.com/en/research-article/volkswagens-long-term-high-manganese-cathode-strategy/23431.
13. Song, J., et al., *Building Better Full Manganese-Based Cathode Materials for Next-Generation Lithium-Ion Batteries.* Electrochemical Energy Reviews, 2023. **6**(1): p. 20.
14. Thapa, A.K., et al., *Mn-Rich NMC Cathode for Lithium-Ion Batteries at High-Voltage Operation.* Energies, 2022. **15**(22): p. 8357.

15. Chen, J., et al., *Critical barriers to successful implementation of earth-abundant, Mn-rich cathodes for vehicle applications and beyond: a detailed study of low SOC impedance.* Journal of The Electrochemical Society, 2021. **168**(8): p. 080506.
16. Gutierrez, A., et al., *Advancing lithium-and manganese-rich cathodes through a combined electrolyte additive/surface treatment strategy.* Journal of The Electrochemical Society, 2019. **166**(16): p. A3896.
17. Gutierrez, A., et al., *Critical Barriers to Successful Implementation of Earth-Abundant, Mn-Rich Cathodes for Vehicle Applications and Beyond: The Effect of Particle Morphology.* Journal of The Electrochemical Society, 2022. **169**(2): p. 020574.
18. Croy, J.R., et al., *Review of the U.S. Department of Energy's "Deep Dive" Effort to Understand Voltage Fade in Li- and Mn-Rich Cathodes.* Accounts of Chemical Research, 2015. **48**: p. 2813 - 2821.
19. Erickson, E.M., et al., *Review-Recent Advances and Remaining Challenges for Lithium Ion Battery Cathodes: II. Lithium-Rich, xLi⊂2⊆MnO⊂3⊆(1-x)LiNi⊂a⊆Co⊂b⊆Mn⊂c⊆O⊂2⊆.* Journal of the Electrochemical Society, 2017. **164**(1): p. A6341-A6348.
20. Gutierrez, A., et al., *Earth-Abundant, Mn-Rich Cathodes for Vehicle Applications and Beyond: Overview of Critical Barriers.* Journal of The Electrochemical Society, 2023.
21. Schipper, F., et al., *Recent advances and remaining challenges for lithium ion battery cathodes.* Journal of The Electrochemical Society, 2016. **164**(1): p. A6220.
22. Xu, G.L., et al., *Challenges and Strategies to Advance High-Energy Nickel-Rich Layered Lithium Transition Metal Oxide Cathodes for Harsh Operation.* Advanced Functional Materials, 2020. **30**(46).
23. Zheng, J., et al., *Li-and Mn-rich cathode materials: challenges to commercialization.* Advanced Energy Materials, 2017. **7**(6): p. 1601284.
24. Pişkin, B., C.S. Uygur, and M.K. Aydınol, *Morphology effect on electrochemical properties of doped (W and Mo) 622NMC, 111NMC, and 226NMC cathode materials.* International Journal of Hydrogen Energy, 2020. **45**(14): p. 7874-7880.
25. Harlow, J.E., et al., *A Wide Range of Testing Results on an Excellent Lithium-Ion Cell Chemistry to be used as Benchmarks for New Battery Technologies.* Journal of the Electrochemical Society, 2019. **166**(13): p. A3031-A3044.
26. Jin, X., et al., *Mesoporous Single-Crystal Lithium Titanate Enabling Fast-Charging Li-Ion Batteries.* Advanced Materials, 2022. **34**(18).
27. Zhang, X.L., et al., *NASICON-Structured LiZr2(PO4)3 Surface Modification Improves Ionic Conductivity and Structural Stability of LiCoO2 for a Stable 4.6 V Cathode.* Acs Applied Materials & Interfaces, 2022. **14**(14): p. 16204-16213.
28. Wang, D., et al., *Growth mechanism of Ni0. 3Mn0. 7CO3 precursor for high capacity Li-ion battery cathodes.* Journal of Materials Chemistry, 2011. **21**(25): p. 9290-9295.
29. Cai, C., H. Dong, and G.M. Koenig Jr, *Anisotropic particle synthesis and characterization for lithium-ion battery electrode materials via precursor precipitate growth inhibitor.* Powder Technology, 2021. **394**: p. 214-224.
30. Hendrickx, M., et al., *The Influence of Synthesis Method on the Local Structure and Electrochemical Properties of Li-Rich/Mn-Rich NMC Cathode Materials for Li-Ion Batteries.* Nanomaterials, 2022. **12**(13): p. 2269.

31. Kumar, R.V., E. Weal, and J.C. Tan. *Dissemination of IT for the Promotion of Materials Science (DoITPoMS): Batteries*. 2004 - 2023; Available from: https://www.doitpoms.ac.uk/tlplib/batteries/printall.php.
32. Rudnicka, E., P. Jakobczyk, and A. Lewandowski, *Thermodynamic and kinetic limits of Li-ion battery operation.* Journal of Energy Storage, 2022. **55**: p. 105747.
33. Urban, A., D.-H. Seo, and G. Ceder, *Computational understanding of Li-ion batteries.* npj Computational Materials, 2016. **2**(1): p. 1-13.
34. Dong, H. and G.M. Koenig, *A review on synthesis and engineering of crystal precursors produced via coprecipitation for multicomponent lithium-ion battery cathode materials.* CrystEngComm, 2020. **22**(9): p. 1514-1530.
35. Dong, H. and G.M. Koenig Jr, *Compositional control of precipitate precursors for lithium-ion battery active materials: role of solution equilibrium and precipitation rate.* Journal of Materials Chemistry A, 2017. **5**(26): p. 13785-13798.
36. Feng, Z., et al., *In situ monitoring of the growth of nickel, manganese, and cobalt hydroxide precursors during co-precipitation synthesis of Li-ion cathode materials.* Journal of The Electrochemical Society, 2018. **165**(13): p. A3077.
37. Kim, U.-H., et al., *Heuristic solution for achieving long-term cycle stability for Ni-rich layered cathodes at full depth of discharge.* Nature energy, 2020. **5**(11): p. 860-869.
38. Riewald, F., et al., *The LiNiO2 Cathode Active Material: A Comprehensive Study of Calcination Conditions and their Correlation with Physicochemical Properties Part II. Morphology.* Journal of The Electrochemical Society, 2022. **169**(2): p. 020529.
39. Wolfman, M., et al., *The importance of surface oxygen for lithiation and morphology evolution during calcination of high-nickel NMC cathodes.* Advanced Energy Materials, 2022. **12**(16): p. 2102951.
40. Aryal, S., et al., *Roles of Mn and Co in Ni-rich layered oxide cathodes synthesized utilizing a Taylor Vortex Reactor.* Electrochimica Acta, 2021. **391**: p. 138929.
41. Garcia, J.C., et al., *Predicting morphological evolution during coprecipitation of MnCO3 battery cathode precursors using multiscale simulations aided by targeted synthesis.* Chemistry of Materials, 2020. **32**(21): p. 9126-9139.
42. Navrotsky, A., *Nanoscale effects on thermodynamics and phase equilibria in oxide systems.* ChemPhysChem, 2011. **12**(12): p. 2207-2215.
43. Pimenta, V., et al., *Synthesis of Li-Rich NMC: A Comprehensive Study.* Chemistry of Materials, 2017. **29**(23): p. 9923-9936.
44. Kolthoff, I., *Theory of coprecipitation. The formation and properties of crystalline precipitates.* The Journal of Physical Chemistry, 1932. **36**(3): p. 860-881.
45. Yang, Y.S., et al., *Low-Temperature Synthesis of Hierarchical Amorphous Basic Nickel Carbonate Particles for Water Oxidation Catalysis.* Chemsuschem, 2015. **8**(13): p. 2193-2197.
46. Barai, P., et al., *Multiscale computational model for particle size evolution during coprecipitation of Li-ion battery cathode precursors.* The Journal of Physical Chemistry B, 2019. **123**(15): p. 3291-3303.
47. Kashchiev, D. and G. Van Rosmalen, *Nucleation in solutions revisited.* Crystal Research and Technology: Journal of Experimental and Industrial Crystallography, 2003. **38**(7-8): p. 555-574.

48. Richens, D.T., *Ligand substitution reactions at inorganic centers.* Chemical Reviews, 2005. **105**(6): p. 1961-2002.
49. Robinson, J.P. and G.M. Koenig Jr, *Tuning solution chemistry for morphology control of lithium-ion battery precursor particles.* Powder Technology, 2015. **284**: p. 225-230.
50. Ngoepe, N., et al., *The effects of process parameters on the properties of manganese-rich carbonate precursors: A study of co-precipitation synthesis using semi-batch reactors.* Chemical Engineering Science, 2021. **241**: p. 116694.
51. JEOL. *JCM-6000Plus Versatile Benchtop SEM*. 2023; Available from: https://www.jeol.com/products/scientific/sem/JCM-6000Plus.php.
52. Wen, J. *CENTER FOR NANOSCALE MATERIALS: Electron and X-ray Microscopy Capabilities*. 2023 [cited 2023; Available from: https://www.anl.gov/cnm/electron-and-xray-microscopy-capabilities.
53. Prescher, C. and V.B. Prakapenka, *DIOPTAS: a program for reduction of two-dimensional X-ray diffraction data and data exploration.* High Pressure Research, 2015. **35**(3): p. 223-230.
54. Kresse, G. and J. Furthmuller, *Efficiency of ab-initio total energy calculations for metals and semiconductors using a plane-wave basis set.* Computational Materials Science, 1996. **6**(1): p. 15-50.
55. Kresse, G. and J. Hafner, *Ab initio molecular dynamics for liquid metals.* Physical review B, 1993. **47**(1): p. 558.
56. Perdew, J.P., K. Burke, and M. Ernzerhof, *Generalized gradient approximation made simple.* Physical Review Letters, 1996. **77**(18): p. 3865-3868.
57. Blochl, P.E., *Projector Augmented-Wave Method.* Physical Review B, 1994. **50**(24): p. 17953-17979.
58. Ceder, G., et al., *Identification of cathode materials for lithium batteries guided by first-principles calculations.* Nature, 1998. **392**(6677): p. 694-696.
59. van Bommel, A. and J.R. Dahn, *Analysis of the Growth Mechanism of Coprecipitated Spherical and Dense Nickel, Manganese, and Cobalt-Containing Hydroxides in the Presence of Aqueous Ammonia.* Chemistry of Materials, 2009. **21**(8): p. 1500-1503.
60. Wang, D.P., et al., *Synthesis of high capacity cathodes for lithium-ion batteries by morphology-tailored hydroxide co-precipitation.* Journal of Power Sources, 2015. **274**: p. 451-457.
61. Xiang, Y.H., Z.L. Yin, and X.H. Li, *Synthesis and characterization of manganese-, nickel-, and cobalt-containing carbonate precursors for high capacity Li-ion battery cathodes.* Journal of Solid State Electrochemistry, 2014. **18**(8): p. 2123-2129.
62. Qiu, L., et al., *Exposing microstructure evolution of Ni-Rich Ni-Co-Al hydroxide precursor.* Chemical Engineering Science, 2021. **233**.
63. Lee, M.H., et al., *Synthetic optimization of Li[Ni1/3Co1/3Mn1/3]O-2 via co-precipitation.* Electrochimica Acta, 2004. **50**(4): p. 939-948.
64. Zhang, S., et al., *An improved carbonate co-precipitation method for the preparation of spherical Li[Ni1/3Co1/3Mn1/3]O-2 cathode material.* Journal of Alloys and Compounds, 2009. **484**(1-2): p. 519-523.

65. Bombaˇc, D., *Atomistic Simulations of Precipitation Kinetics in Multicomponent Interstitial/Substitutional Alloys*, in *Department of Materials and Metallurgy*. 2012, University of Ljubljana.
66. Rak, M., M. Izdebski, and A. Brozi, *Kinetic Monte Carlo study of crystal growth from solution.* Computer Physics Communications, 2001. **138**(3): p. 250-263.
67. Karthika, S., T.K. Radhakrishnan, and P. Kalaichelvi, *A Review of Classical and Nonclassical Nucleation Theories.* Crystal Growth & Design, 2016. **16**(11): p. 6663-6681.
68. Mullin, J.W., *Crystallization*. 4th ed. 2001, Oxford ; Boston: Butterworth-Heinemann. xv, 594 p.
69. Verma, A., et al., *Galvanostatic Intermittent Titration and Performance Based Analysis of LiNi0.5Co0.2Mn0.3O2 Cathode.* Journal of the Electrochemical Society, 2017. **164**(13): p. A3380-A3392.
70. Cambridge, U.o. *Mass Transport*. 2023; Available from: https://www.ceb.cam.ac.uk/research/groups/rg-eme/Edu/mass-transport.
71. Deen, W.M., *Analysis of transport phenomena*. Topics in chemical engineering. 1998, New York: Oxford University Press. xix, 597 p.
72. Helmy, M. *Fundamentals of Mass Transfer*. Available from: https://www.kau.edu.sa/Files/0060757/Subjects/1%20Fundamentals.pdf.
73. Schwarze, J., et al., *Attachment and Detachment of Particles from a Surface under Shear Flow.* Journal of Physical Chemistry C, 2019. **123**(13): p. 8153-8159.
74. Serra, T., J. Colomer, and X. Casamitjana, *Aggregation and breakup of particles in a shear flow.* Journal of Colloid and Interface Science, 1997. **187**(2): p. 466-473.
75. Harshe, Y.M. and M. Lattuada, *Breakage Rate of Colloidal Aggregates in Shear Flow through Stokesian Dynamics.* Langmuir, 2012. **28**(1): p. 283-292.
76. Guo, M.M., et al., *Preparation of Small-Particle and High-Density Cobalt Carbonate Using a Continuous Carbonate Precipitation Method and Evaluation of Its Growth Mechanism.* Materials, 2019. **12**(20).
77. Goldstein, J.I., et al., *Scanning Electron Microscopy and X-Ray Microanalysis*. 2018, Springer New York : Imprint: Springer,: New York, NY. p. 1 online resource (XXIII, 550 pages 546 illustrations, 409 illustrations in color.
78. Shu, Q.F., et al., *Modelling the Nucleation, Growth and Agglomeration of Alumina Inclusions in Molten Steel by Combining Kampmann-Wagner Numerical Model with Particle Size Grouping Method.* Metallurgical and Materials Transactions B-Process Metallurgy and Materials Processing Science, 2021. **52**(3): p. 1818-1829.
79. Ring, T.A. *Nucleation. Growth and Agglomeration during Precipitation of Powders*. in *Proceedings of Second World Congress PARTICLE TECHNOLOGY*. 1990. Kyoto, Japan.
80. Orrite, S.D., S. Stoll, and P. Schurtenberger, *Off-lattice Monte Carlo simulations of irreversible and reversible aggregation processes.* Soft Matter, 2005. **1**(5): p. 364-371.
81. Roberts, P.J. and D.R. Webster, *Turbulent diffusion*. 2002, ASCE Press, Reston, Virginia. p. 7-47.

List of Figures

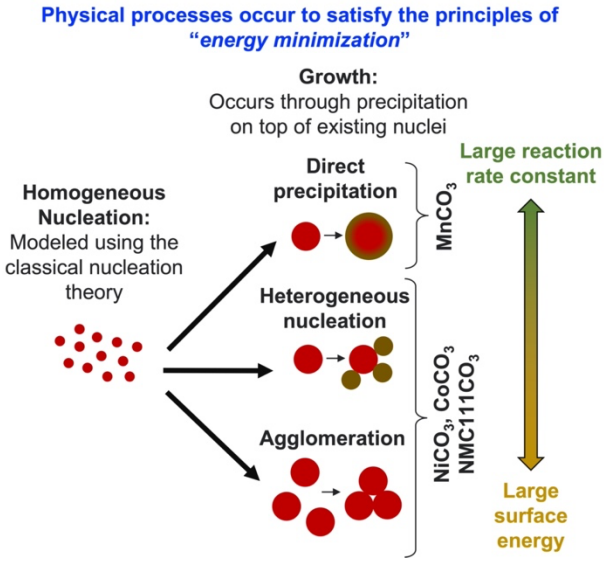

Figure: 1. Schematic Demonstration of the two physical phenomena, namely "nucleation" and "growth", that contributes to the formation of the cathode precursors. Growth of the transition metal carbonate precipitates can occur through three mechanisms, direct precipitation, heterogeneous nucleation on particle surface, and agglomeration. Competition between the "reaction rate constant" and "surface energy" dictates the dominant growth mechanism.

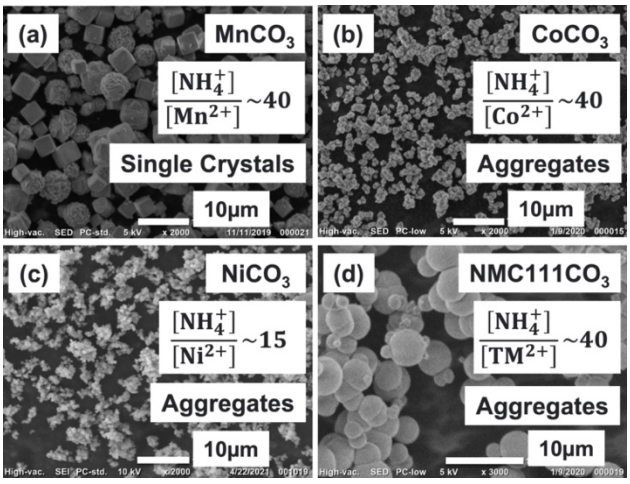

Figure: 2. Microstructure of different transition metal carbonate precursor particles as visualized using benchtop scanning electron microscope (SEM). (a) $MnCO_3$ demonstrates single or pseudo-single crystalline features, and the particle size is around 6 μm – 7 μm. (b) $CoCO_3$ forms smaller aggregates with particle size around 2 μm. (c) $NiCO_3$ demonstrates similar random shaped aggregates with particle size in the range of 0.5 μm – 2 μm. (d) (NMC111)CO_3 shows spherical aggregates with extremely smooth surface and particle size ranging between 5 μm – 6 μm. While precipitating the carbonate precursor particles for obtaining these images, the total transition metal concentration was maintained at 4.5 mM. For Mn, Co and NMC111 carbonates, the ammonium-bicarbonate over transition metal ratio was maintained at 40:1; whereas, for Ni carbonates the concentration of ammonium bicarbonate was maintained at a level 15 times larger than the Ni concentration.

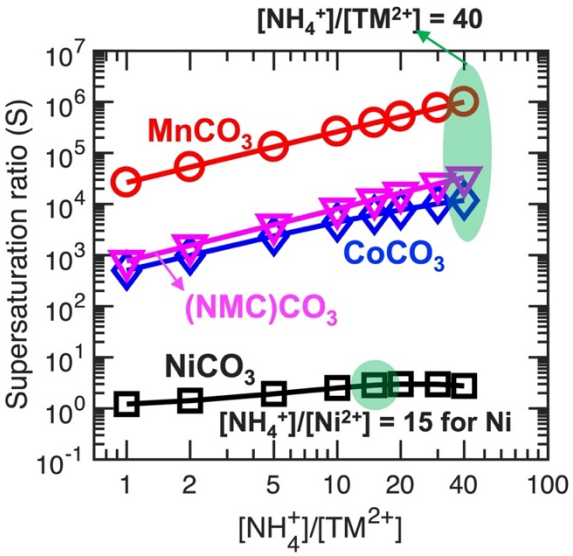

Figure: 3. Variation in supersaturation for transition metal carbonates with increasing ammonia over transition metal ratio. All the supersaturation ratios were obtained by solving a set of mass balance equations that uses thermodynamic equilibrium constants. The total transition metal concentration is maintained at 4.5 mM while conducting this analysis. Ammonia is added within the solution in the form of ammonium bicarbonate (NH_4HCO_3), and the bicarbonate anions (HCO_3^-) decompose and provide the carbonates (CO_3^{2-} ß) necessary for precipitating the transition metal carbonates. Increasing the amount of ammonia requires addition of more ammonium bicarbonates, which enhances the amount of carbonate anions, and effectively leads to an increase in supersaturation ratio for the transition metal carbonates. This trend is evident for Mn, Co and (NMC) carbonates. However, for Ni-carbonates, increasing the amount of ammonia leads to the formation of excessive Ni-ammonia complex ($[Ni(NH_4)_n]^{2+}$), which decreases the amount of free Ni^{2+} ions within the solution, and the supersaturation ratio decreases.

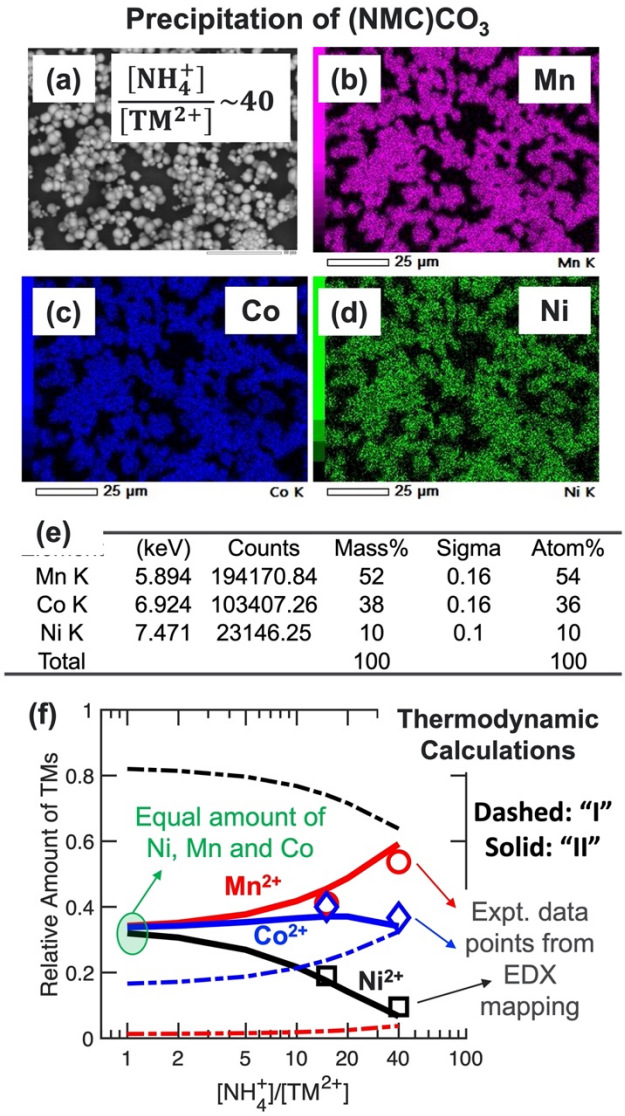

Figure: 4. Elucidation of transition metal carbonate precipitation reaction mechanism from the relative amounts of precipitated transition metals in NMC-carbonates. (a) SEM image of the precipitated NMC-carbonates, while maintaining ammonia over transition metal ratio of 40:1. (b) – (d) Distribution of the Mn, Co, and Ni within the precipitate. Uniform distribution of the transition metals indicates similar composition of Mn, Co, and Ni within all the particles. (e) Mass and atomic percentage of Mn, Co, and Ni within the precipitate. It is evident that maximum amount of Mn is deposited, then Co, and very few Ni gets precipitated. It is possible to form transition metal carbonates in two possible ways: i) Precipitation due to reaction between carbonate anions and transition metal ammonia complex, and ii) Direct precipitation due to reaction between metal cations and carbonate anions. (f) Computationally predicted relative amount of free transition metals floating within the solution is plotted with respect to ammonia over transition metal ratio ($[NH_4^+]/[TM^{2+}]$). The experimentally observed relative amount of Mn, Co, and Ni ions within the NMC-carbonate precipitates are demonstrated by the symbols as obtained at 15:1 and 40:1 ratios of ammonia over transition metal. Extremely good correlation between the computational prediction and experimental observation indicates that precipitation of transition metal carbonates occurs due to reaction between the free transition metal cations and carbonate anions. If precipitation occurred through the reaction between metal ammonia complex and carbonate anions, then the relative amount of transition metals within the precipitates are shown by the dashed line. In the present calculations, even though equal amount of Mn,

Co and Ni salts were used, very different amount of the three transition metals were precipitated. To obtain equal amount of Mn, Co, and Ni, it is suggested to operate at ammonia over transition metal ratio around 1.0, which is highlighted by the green circle.

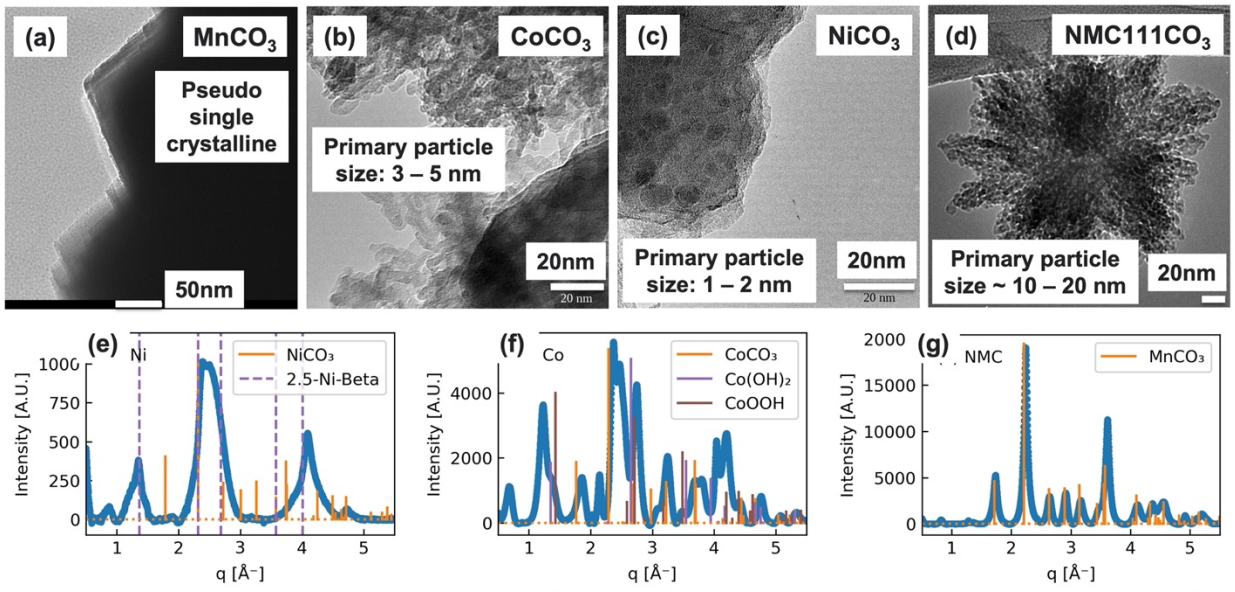

(h) **DFT Calculations**

	$MnCO_3$	$NiCO_3$	$CoCO_3$
Minimum energy surface type	(102)	(102)	(102)
Surface energy (J/m^2)	1.05	1.79	1.53

(i) **Characterization of precipitates: XRD/EDX analysis**

Material	Primary particle size: FWHM of XRD (nm)	Ni:Mn:Co (from EDX mapping)
$NiCO_3$	1.4	99:0:1
$CoCO_3$	3.9	1:0:99
$NMC111CO_3$	8.92	19:41:40

Figure: 5. Primary particle microstructures obtained for different transition metal carbonates. Precipitation reactions are conducted in a batch reactor at 50°C with total transition metal concentration of 4.5 mM and ammonia over transition metal ratio ($[NH_4]$:[TM]) of 40:1. For the case of $NiCO_3$ only, $[NH_4]$:[TM] ratio is maintained at 15:1 for maximizing transition metal carbonate supersaturation ratio. (a) Primary particle of $MnCO_3$ that shows pseudo single crystalline morphology (see Garcia et al., *Chem Mater* 2020 9126 – 9139). The particles also appear to take their minimum energy Wulff configuration. (b) Primary particle morphology of $CoCO_3$ demonstrating extremely small primary particles of size 3 – 5 nm aggregated together that forms a rough surface. (c) 1 – 2 nm sized primary particles of $NiCO_3$ that form larger aggregates with a smooth surface. (d) Primary particle aggregates of $NMC111CO_3$ consisting of 10 – 20 nm sized crystallites, and the surface of the aggregates appear to be rough in nature. For $CoCO_3$, $NiCO_3$ and $NMC111CO_3$, the primary particles do not demonstrate any regular shape, and appears to be spherical. (e – g) Powder X-ray diffraction of representative coprecipitation products. Diffraction patterns were measured using synchrotron radiation (λ = 0.45175Å) on precipitated products formed from solutions containing (e) $NiSO_4$, (f) $CoSO_4$, and (g) a mixture of $NiSO_4$, $MnSO_4$, and $CoSO_4$ mixed in equal ratio. All solutions contained 4.5 mM transition metal, and $[NH_4^+]$:$[TM^{2+}]$ ratio is maintained at 15:1 for precipitating $NiCO_3$ and $NMC111CO_3$, and 40:1 for precipitating $CoCO_3$. Vertical lines show expected reflections for

the corresponding transition metal carbonates: (e) $NiCO_3$ ICSD 61067, Ni precipitate,[45] (f) $CoCO_3$ ICSD 61066, $Co(OH)_2$ ICSD 257275, CoOOH ICSD 20566, (g) $MnCO_3$ ICSD 8433. (h) According to the computational simulations conducted at lower length scale using the Density Functional Theory (DFT), all the three individual transition metal carbonates demonstrate (102) as the minimum energy surface. The minimum surface energies of $MnCO_3$, $CoCO_3$ and $NiCO_3$ are 1.05 J/m^2, 1.53 J/m^2 and 1.79 J/m^2, respectively. As already shown in Figures 5(a – d), except $MnCO_3$, none of the transition metal carbonates demonstrate the minimum energy Wulff configuration. (i) A table demonstrating the primary particle size and relative amount of TM distribution in $NiCO_3$, $MnCO_3$ and $NMC111CO_3$ precipitates. The primary particle sizes are extracted using the full width half maximum (FWHM) of the individual XRD peaks shown in Figure 5(e – g). The relative amount of Ni, Mn, and Co present in the precipitate is estimated using EDX mapping techniques.

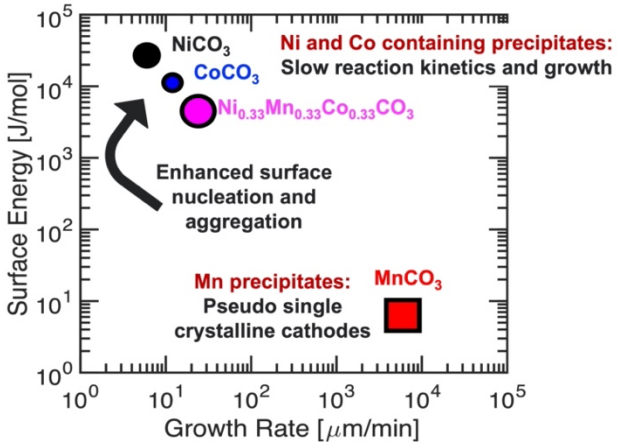

Figure: 6. Change in surface energy of the transition metal carbonate precipitates as compared to their growth rate. $MnCO_3$ demonstrates high reaction rate constants and extremely high supersaturation ratios, which results in very fast growth of the particles. Quick growth also keeps the surface energy of these $MnCO_3$ precipitates low, where agglomeration is not favored (see Garcia et al., *Chem Mater* 2020 9126 – 9139). On the other hand, Ni and Co containing $NiCO_3$, $CoCO_3$, and $NMC111CO_3$ demonstrates slower reaction rate constant, which leads to slower growth of the primary particles through direct precipitation and the individual primary crystallites for these Ni and Co containing precursors is extremely small, in the range of nanometers (see Figure 5). Instead of direct precipitation, Ni and Co containing particles prefer to grow through surface nucleation. Due to the smaller primary particle size of these Ni and Co containing precipitates, they demonstrate higher surface energies, which enhances their propensity to agglomerate during the formation of the secondary particles.

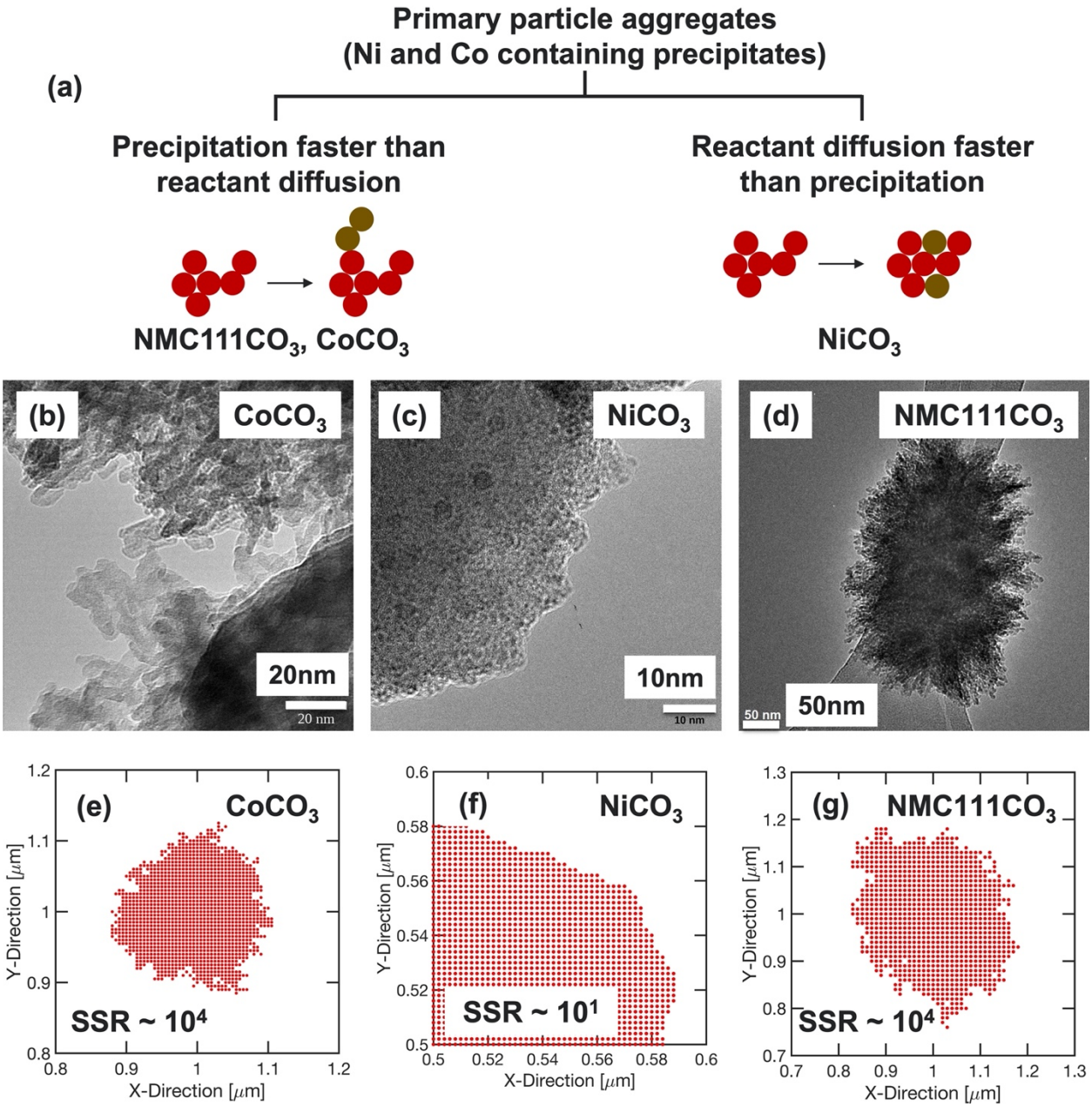

Figure: 7. (a) Schematic representation of the two competing phenomena, diffusion of reactants within solution and precipitation of reactants, that contributes to the determination of the surface morphology of the $TMCO_3$ precipitates. (b – g) High resolution transmission electron microscopy (HR-TEM) image of the aggregated primary particles for different transition metal carbonates, and the corresponding computationally generated microstructures. (b) Primary particles of $CoCO_3$, which is precipitated at transition metal concentration of 4.5 mM and ammonia over transition metal ($[NH_4]$:[TM]) ratio of 40:1. Surface of these $CoCO_3$ precipitates appear to be rough in nature. (c) Primary particle morphology of $NiCO_3$ precipitated at metal concentration 4.5 mM and $[NH_4]$:[TM] ratio of 15:1. For $NiCO_3$, the precipitate surface appears to be smooth. (d) Primary particle microstructures of $NMC111CO_3$ precipitated at total transition metal concentrations of 4.5 mM with $[NH_4]$:[TM] ratio of 40:1. Surface of these precipitates of $NMC111CO_3$ appear to be extremely rough in nature. All these three Ni and Co containing carbonate precipitates are assumed to grow through surface nucleation due to the smaller reaction rate constant and growth rate. (e – g) Simulated primary particle microstructures of $CoCO_3$, $NiCO_3$ and $NMC111CO_3$ using

Monte Carlo based computational frameworks. Precipitation of these transition metal carbonate precursors are assumed to be governed by two different driving forces; (i) Driving force for precipitation, which is dictated by the extent of supersaturation ratio, and (ii) Driving force for surface energy minimization, which occurs through diffusion type mechanisms. As shown in (e) and (g), $CoCO_3$ and $NMC111CO_3$ demonstrates higher supersaturation ratios (SSR ~ 10^4), which leads to larger driving force of precipitation without much room for the surface energy minimization mechanism to kick in. This results in a rougher precipitate morphology for $CoCO_3$ and $NMC111CO_3$. On the contrary, as shown in (f), precipitation of $NiCO_3$ occurs under much lower supersaturation ratios (SSR ~ 10), which minimizes the driving force for precipitation, and allows for reactant diffusion to play a role in minimizing the surface energies. Hence, experimentally observed (see (c)) and computationally predicted (see (f)) precipitates of $NiCO_3$ demonstrate smooth surface.

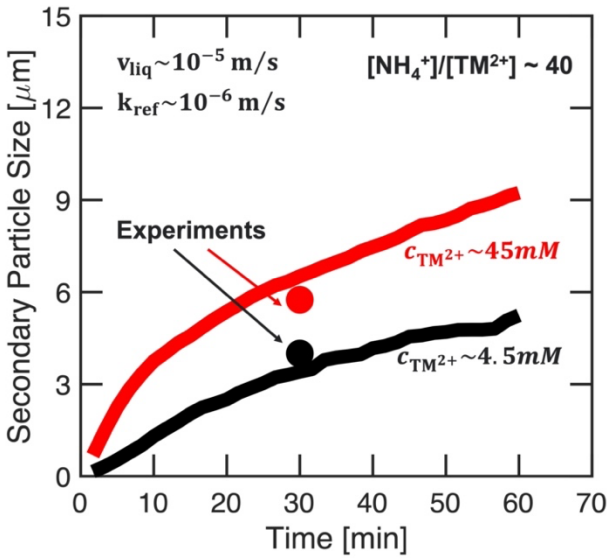

Figure: 8. Secondary particle size of $NMC111CO_3$ as a function of time as predicted by the computational scheme. Evolution of secondary particles are simulated using a combination of mass balance and Kinetic Monte Carlo (KMC) approach for $NMC111CO_3$ only, because realistic cathodes always consist of a combination of the three different transition metals, never the individual end members. Two different transition metal concentrations are considered, 4.5 mM and 45 mM, while the ammonia over transition metal ratio ($[NH_4]$:[TM]) is maintained constant at 40:1. The experimental precipitations are conducted in a batch reactor at 50°C under stirring at 500 rpm. The experimentally observed particle sizes at 4.5 mM and 45 mM transition metal concentrations are denoted by the black and red circles, respectively. The computationally predicted secondary particle sizes are depicted by the black and red solid lines for metal concentrations of 4.5 mM and 45 mM, respectively. The local liquid velocity is assumed to be 10^{-5} m/s and reaction rate constant for the growth of the primary aggregates are assumed to be around 10^{-6} m/s, which is selected to obtain a good fit with the experimental observations.

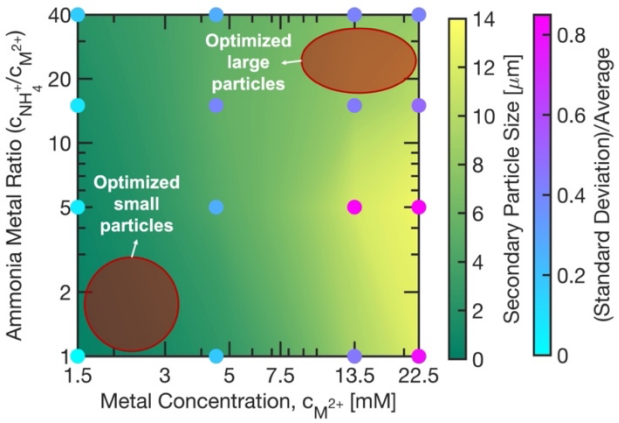

Figure: 9. Phase map between transition metal concentration and ammonia over transition metal ratio ([NH_4]:[TM]) demonstrating variation in secondary particle size as a function of the two abovementioned parameters. In the phase map yellow indicates larger secondary particles whereas green denotes smaller secondary particles. It is evident that increasing metal concentration leads to an increase in the secondary particle size, which can be attributed to enhanced nucleation, agglomeration, and subsequent increase of the secondary particle size. The size distribution is denoted by the standard deviation of the particle size, which is shown by the dots using the colors in the second color bar, where magenta indicates larger size distribution and cyan denotes smaller size distributions. The optimized smaller particles can be obtained under small metal concentrations and smaller magnitudes of ammonia over metal ratios, whereas larger particle sizes with smaller size distribution can be extracted under large transition metal concentration and higher ammonia metal ratios.

TOC Image

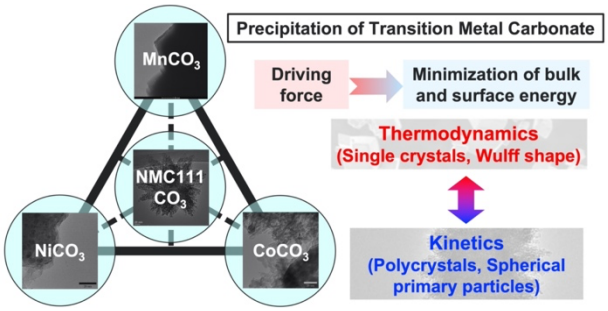

TOC Figure: Schematic representation of the precipitation of different transition metal carbonates, where the major driving force is the minimization of bulk and surface free energy. For thermodynamically dominated precipitates single crystalline particles with Wulff shape are observed, whereas, for kinetically controlled precipitation mechanism polycrystalline precipitates with spherical primary particles are obtained.